Investigating the Circumstellar Environments of Young Stars with the PROMPT Polarimeter

by

Jane A. Moran

A dissertation submitted to the faculty of the University of North Carolina at Chapel Hill in partial fulfillment of the requirements for the degree of Doctor of Philosophy in the Department of Physics & Astronomy.

Chapel Hill

2009

Approved by:

J. Christopher Clemens, Advisor
Wayne A. Christiansen, Reader
Charles R. Evans, Reader
Laura Mersini, Reader
James A. Rose, Reader

ABSTRACT

JANE A. MORAN: Investigating the Circumstellar Environments of Young Stars with the PROMPT Polarimeter
(Under the Direction of J. Christopher Clemens)

We have designed and built a prototype imaging polarimeter for use on the PROMPT robotic telescopes located at the Cerro Tololo International Observatory. The polarimeter uses a Fresnel rhomb and wollaston prism to image two orthogonal polarization states onto a single CCD chip, with an image field of view of 10x4.5 arcmin. Using the polarimeter, we have investigated the circumstellar regions of 11 Herbig Ae/Be stars, and done extensive follow-up observations of 3 stars of interest: KK Oph, a well-studied star with previously limited polarimetric data; NX Pup, a star known to vary photometrically but with previously unknown polarimetric variability; and SS7344, a star with very limited previous photometric data and no prior polarimetric data. We have found polarimetric and photometric variations in KK Oph and NX Pup that are consistent with models of dust obscuration. Both KK Oph and NX Pup show an increase in polarization accompanied by a decrease in visual magnitude and a reddening. However, neither star shows the "blueing" at deep minima and maximum polarization characteristic of the UXor classification of stars. We have demonstrated that SS7344 has an intrinsic polarization, but does not display the photometric and polarimetric variations expected from a young star with an evolving circumstellar environment, indicating that this object either has a disk seen in an orientation that has little inclination, or one with no appreciable puffed-up inner rim.

ACKNOWLEDGMENTS

To Chris, Without your help and support I never would have made it this far. I know that I wasn't always the easiest student to mentor, but you stuck with me until the end. I thank you for your never-ending patience and for your encouragement.

To Ed and Carol Smithwick, I am forever grateful for your generous endowment of the Royster Society of Fellows, which sponsored me in my final year with a Dissertation Completion Fellowship. Your generosity vastly impacted my life in a positive way.

To Susan, many thanks for all the discussions about polarimetry. Your input was invaluable in the preparation of this thesis.

To Hugon, you were always solid in your support for me, and just knowing that you would always be there to listen has made all the difference. Thank you for everything.

To the Shop Guys: Cliff, Phil, Neal and Steve, I've lost track of the number of times that I came down to the shop in a panic with partially drawn figures in my hand of parts that needed to be finished the next day. Every time, you seemed to take it in stride, and produced professional quality parts on impossible time-scales. Thank you for all your work, and for your patience. Thanks to you the polarimeter is not only functional, but it looks great too.

To Mr. Morton, my high school physics teacher, for getting me excited about physics and for teaching me the basics so thoroughly that I was bound to succeed.

To Melissa, for all the trips to PARI that got the PROMPT project rolling. I hope that you continue to enjoy a successful career.

To Calin, you have helped me in so many ways, from helping me study for the qualifying exams to fixing computers offering me advice and encouragement over a cup of coffee. Thanks for being such a great friend.

To Mom, thank you for always being my biggest fan and a constant support in my life.

To Dad, thank you for providing me with inspiration from a young age and for instilling in me a deep love of science and discovery.

To Michael, for never once complaining about the sacrifices that had to be made for me to get this far, and for never wavering in your love for me. You mean the world to me.

Jane A. Moran.

July 20, 2009

CONTENTS

LIST OF TABLES

LIST OF FIGURES

LIST OF ABBREVIATIONS

CTIO	Cerro Tololo International Observatory
DEC	Declination
GRB	Gamma-Ray Burst
HAEBE	Herbig Ae/Be
HH	Herbig-Haro
IRAF	Image Reduction and Analysis Facility
ISM	Interstellar Medium
LTVP	Long-Term Variability Project
NIR	Near Infrared
OTA	Optical Tube Assembly
PA	Position Angle
PMS	Pre-Main Sequence
PROMPT	Panchromatic Robotic Optical Monitoring and Polarimetry Telescopes
TOO	Target of Opportunity
RA	Right Ascension

Chapter 1

Introduction

Like many things in life, this thesis is divided into two separate, yet equally important parts. It is primarily an instrumentation project, and much of the discussion that follows relates directly to the instrument in question: the PROMPT polarimeter. We discuss the concept, design, assembly and testing of this instrument as well as methods for using it and analyzing the data that it produces. As a complementary aspect to the instrumentation project, the second part of this work is devoted to the investigation of the understanding of the structure of circumstellar disks surrounding young stars, using the PROMPT polarimeter. This is a problem of particular interest lately, as it relates to an understanding of planetary formation in young star systems. We address this problem by presenting new polarimetry data obtained with the PROMPT polarimeter, and we discuss its implications for disk structure. We begin, though, with an overview of the field of polarimetry.

1.1 Motivation

The field of astronomy is very much dependent on an astronomer's ability to interpret light. Almost everything that we know about the Universe comes from information that we have gleaned from the careful analysis of all of the properties of electromagnetic radiation. It is for that reason that it is surprising that a certain property of light, it's *polarization*, is neglected by all but a few astronomers.

The reason that the polarization of light isn't widely used as a tool for studying astronomical systems is three-fold. Firstly, the tools used to study the polarization of light - polarimeters - are not widely available for use. There are virtually no telescopes in the world that are entirely devoted to polarimetry work, and for those telescopes that have a polarimeter available for occasional use, the instrument change is time-consuming and technical.

The second strike against polarimetry is the specialization needed to analyze and interpret the data. Polarimetry analysis requires its own set of techniques and skills, and although many of those techniques are closely related to those found in other areas of image analysis, the differences are just large enough to be daunting to the inexperienced would-be polarimetrist.

The final blow to polarimetry arises as a consequence of the first two, and practically seals the fate of this branch of astronomy. Because of the rarity of reference to polarimetry in scientific studies, it is easily forgotten, neglected, or dismissed as unimportant to our overall understanding of a system being studied.

In this thesis, we aim to illustrate the importance and relevance of polarimetric studies for a variety of different systems. We will begin the discussion with a review of some of the most common concepts in polarimetry.

1.2 Basic Concepts in Polarimetry

In this section we aim to outline some of the basic properties of polarimetry and the notations that will be used throughout this work.

1.2.1 The Stokes Parameters

The Stokes parameters are used to define the degrees of linear and circular polarization in a light wave. The equations that follow use the notation of Jackson (1975), and a more detailed derivation of the parameters can be found there.

The most general homogeneous monochromatic plane wave can be described with

the aid of a set of real mutually orthogonal unit vectors $(\boldsymbol{\epsilon}_1, \boldsymbol{\epsilon}_2, \boldsymbol{n})$, shown in figure 1.1. The vectors $\boldsymbol{\epsilon}_1$ and $\boldsymbol{\epsilon}_2$ define the directions of the electric and magnetic field vectors. The propagation vector, $\boldsymbol{k} = k\boldsymbol{n}$, describes the direction, $\boldsymbol{n}$, and the magnitude, $k = \omega/c$ of the propagation of the electromagnetic plane wave.

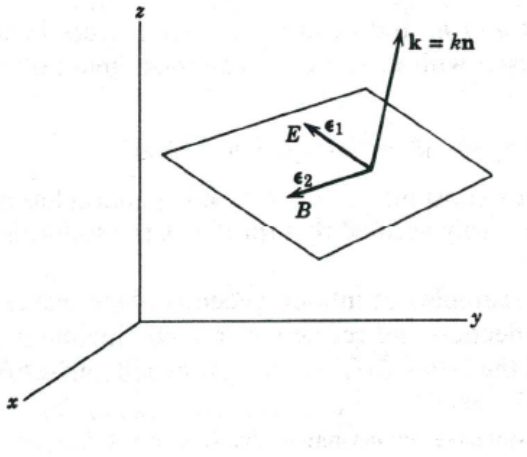

Figure 1.1 The propagation vector $\mathbf{k}$ and the two orthogonal polarization vectors $\boldsymbol{\epsilon}_1$ and $\boldsymbol{\epsilon}_2$. Figure is from Jackson (1975).

A plane wave with its electric field vector always in the direction $\boldsymbol{\epsilon}_1$ is said to be linearly polarized with a polarization vector $\boldsymbol{\epsilon}_1$. Similarly, a plane wave with its electric field vector always in the direction $\boldsymbol{\epsilon}_2$, is linearly polarized with a polarization vector $\boldsymbol{\epsilon}_2$, and is linearly independent of the first.

Thus, the two waves,

$$\begin{aligned} \boldsymbol{E}_1 &= \boldsymbol{\epsilon}_1 E_1 e^{i\boldsymbol{k}\cdot\boldsymbol{x}-\omega t} \\ \boldsymbol{E}_2 &= \boldsymbol{\epsilon}_2 E_2 e^{i\boldsymbol{k}\cdot\boldsymbol{x}-\omega t} \end{aligned} \tag{1.1}$$

with

$$\boldsymbol{B}_j = \sqrt{\mu\epsilon}\frac{\boldsymbol{k}\times\boldsymbol{E_j}}{k}, \qquad j = 1, 2 \tag{1.2}$$

can be combined to give the most general form of a homogeneous plane wave propagating in the direction $\boldsymbol{k} = k\boldsymbol{n}$:

$$\boldsymbol{E}(\boldsymbol{x},t) = (\boldsymbol{\epsilon}_1 E_1 + \boldsymbol{\epsilon}_2 E_2) e^{i\boldsymbol{k}\cdot\boldsymbol{x} - i\omega t} \tag{1.3}$$

Note that here, the amplitudes E_1 and E_2 are complex numbers, since there may be a phase difference between waves of different linear polarization.

If E_1 and E_2 have the same phase, then equation 1.3 represents a linearly polarized wave, with its polarization vector making an angle of $\theta = \tan^{-1}(E_2/E_1)$ and a magnitude of $E = \sqrt{E_1^2 + E_2^2}$.

If E_1 and E_2 have different phases, then the wave is elliptically polarized. Circular polarization occurs in the special case where E_1 and E_2 have the same magnitude, but differ in phase by $90°$.

Thus far, the details of only the simplest (monochromatic) electromagnetic waves have been described. In practice, however, it is much more common to encounter polychromatic light, rather than the simple case of monochromatic waves. As long as the hypotheses of linearity, stationarity and continuity hold, a polychromatic light beam can be considered as a superposition of monochromatic plane waves of frequencies in the interval of width $\Delta\omega$ around a central frequency ω_0. In this case, the x (and y) component of a polychromatic beam streaming along the z-axis can be put in the form:

$$E_x(t) = [\varepsilon_x(t) e^{i\phi_x(t)}] e^{-i\omega_0 t} \tag{1.4}$$

which is a monochromatic plane wave of frequency equal to the mean frequency, modulated by a (complex) amplitude that varies with time. The values in equation 1.4 are defined as follows:

$$\begin{aligned} \varepsilon_x(t) &= \sqrt{E_x(t) E_x^*(t)} = |E_x(t)| \\ \phi_x(t) &= \omega_0 t + \tan^{-1}\left\{ \frac{Im[E_x(t)]}{Re[E_x(t)]} \right\}. \end{aligned} \tag{1.5}$$

In order to generate expressions such as equations 1.3 and 1.4, it is necessary to already have knowledge of the polarization properties of a wave, yet in practice it is

more often the case that an observer is trying to deduce the polarization properties from intensity measurements alone. It was for this reason that G. G. Stokes proposed the four Stokes parameters in 1852. To simplify the notation, we will define the direction of propagation of the radiation as the z-axis. We then begin by defining each of the scalar coefficients in equation 1.3 as a magnitude times a phase factor:

$$E_1 = A_1 e^{i\delta_1}, \qquad E_2 = A_2 e^{i\delta_2} \tag{1.6}$$

Then in the monochromatic case the Stokes parameters become [1]:

$$\begin{aligned} I &= |\boldsymbol{\epsilon}_1 \cdot \boldsymbol{E}|^2 + |\boldsymbol{\epsilon}_2 \cdot \boldsymbol{E}|^2 = A_1^2 + A_2^2 \\ Q &= |\boldsymbol{\epsilon}_1 \cdot \boldsymbol{E}|^2 - |\boldsymbol{\epsilon}_2 \cdot \boldsymbol{E}|^2 = A_1^2 - A_2^2 \\ U &= 2Re[(\boldsymbol{\epsilon}_1 \cdot \boldsymbol{E}) * (\boldsymbol{\epsilon}_2 \cdot \boldsymbol{E})] = 2A_1 A_2 \cos(\delta_2 - \delta_1) \\ V &= 2Im[(\boldsymbol{\epsilon}_1 \cdot \boldsymbol{E}) * (\boldsymbol{\epsilon}_2 \cdot \boldsymbol{E})] = 2A_1 A_2 \sin(\delta_2 - \delta_1) \end{aligned} \tag{1.7}$$

While in the polychromatic case, the Stokes parameters are defined as:

$$\begin{aligned} I &= \kappa(\langle \varepsilon_x^2 \rangle + \langle \varepsilon_y^2 \rangle) \\ Q &= \kappa(\langle \varepsilon_x^2 \rangle - \langle \varepsilon_y^2 \rangle) \\ U &= 2\kappa \langle \varepsilon_x \varepsilon_y \cos\phi(t) \rangle \\ V &= 2\kappa \langle \varepsilon_x \varepsilon_y \sin\phi(t) \rangle \end{aligned} \tag{1.8}$$

As can be seen in equations 1.7 and 1.8, the parameter I measures the relative intensity of the wave. The parameter Q is the difference between the linear x polarization and the linear y polarization, while the parameters U and V carry the phase information.

The Stokes parameters can be described in another way that does not rely on electromagnetic theory and that serves to illustrate how the parameters are derived from physical observations with the polarimeter (Hecht 1998).

Imagine that we are in possession of a set of four filters, each of which, when illuminated with unpolarized light, will transmit half the incident light, discarding

[1] The Stokes parameters are also sometimes referred to by the labels s_0, s_1, s_2, s_3

the other half. Suppose now that the first filter is simply isotropic, passing all states equally, while the second and third filters are linear polarizers whose transmission axes are horizontal and at $+45°$ (diagonal along the first and third quadrants) respectively. The last filter is a circular polarizer opaque to left-circularly polarized light. Each of these four filters is placed alone in the path of the beam under investigation, and the transmitted irradiances I_0, I_1, I_2, I_3 are measured. The operational definition of the Stokes parameters is then given by the following relations:

$$\begin{aligned} I &= 2I_0 \\ Q &= 2I_1 - 2I_0 \\ U &= 2I_2 - 2I_0 \\ V &= 2I_3 - 2I_0 \end{aligned} \tag{1.9}$$

It is clear by this definition that the parameter I represents the total intensity of the beam, while Q and U describe the linear polarization of the beam. The parameter V describes the circular polarization.

Notice also, that under both definitions of the Stokes parameters, the relation

$$I^2 \geq Q^2 + U^2 + V^2 \tag{1.10}$$

is true.

1.2.2 Astronomical Polarimetry

In this section we outline some of the processes that produce a polarization signature in an astronomical source, with particular attention to those that will be relevant later on in this thesis.

A number of polarimetric processes encountered in astronomy are listed in table 1.1. In chapters 4 and 5, we will discuss the main scientific objective of this thesis - an investigation of the circumstellar disks of young, intermediate-mass stellar objects: Herbig Ae/Be stars. These objects display intrinsic polarizations due (in at least some cases) to the reflection of stellar radiation off of the dusty disks that surround the stars.

Table 1.1 Polarimetric Processes encountered in Astronomy

Process	Caused By	Seen In
Extinction	Aligned Dust Grains	Interstellar Polarization
Scattering	Dust	Reflection Nebulae, T-Tauri Stars
Scattering	Rayleigh	Cool Stars
Scattering	Electron	Hot Stellar Envelopes
Scattering	Resonance / Raman Line	Comet, Sun / Symbiotic
Emission	Aligned Dust (Thermal)	Molecular Clouds (IR)
Emission	Cyclotron / Synchrotron	AM Her, Blazers, GRBs

Current research involving these objects relates to determining the exact nature of the disks - their shape, size, and composition. One aspect of the problem that makes it particularly interesting is the complementary problem regarding how planet formation occurs in young star systems. By probing the structure of young stellar disks with polarimetry measurements, we hope to come to a better understanding of the physics that directs disk, and eventually, planetary formation.

The processes that cause the polarization of light in this context are the scattering and extinction of light by dust. Dust causes an observed polarization with a position angle that is generally either perpendicular or parallel to the scattering plane - this concept will be explored in more detail in the following sections.

1.2.3 Polarization by Dust Scattering and Obscuration

The properties of reflected and refracted light at a surface between two dielectric media can be divided into two classes. The kinematic properties are the well known relations that the angle of reflection equals the angle of incidence and Snell's law, describing the angle of refraction in terms of the ratio of the indices of refraction of the two media. The dynamic properties of reflected and refracted light are the

change in intensities that occur when light is either reflected or refracted, as well as the changes in phase and polarization of that radiation (Jackson 1975). It is to these dynamic properties that we turn now.

The polarization of light by reflection from a surface arises due to the need to satisfy the boundary conditions of the Maxwell equations - normal components of $\boldsymbol{D}$ and $\boldsymbol{B}$ are continuous while tangential components of $\boldsymbol{E}$ and $\boldsymbol{H}$ are continuous. By considering the special cases where the polarization is either perpendicular or parallel to the plane of incidence, it can be shown that both the amplitudes and polarizations of reflected and refracted light are well defined quantities when properties of the incident plane wave (its amplitude and wave vector, E_0 and $\boldsymbol{k}$), and of the media in question (the permeabilities and permittivities, μ and ϵ), are known (Jackson 1975). More general cases can be constructed by considering linear superpositions of the two special cases. The equations that describe these properties are known as the Fresnel formulae.

In practice, determining the expected polarization and intensity variations due to the obscuration and/or scattering by dust is not such a straightforward task, due partially to the fact that the exact nature of the dust grains (their size and chemical composition) is generally not known, nor is the geometry of the dusty region, and due also to the difficulty of solving the equations of radiative transfer for a large, thick, dusty region with multiple scattering (Whitney & Hartmann 1992). In general, theoretical scattering models are constructed by numerical methods, such as a Monte Carlo method, in which the parameters pertaining to the nature of the dust and the geometry of the dusty region may be varied to fit with observations.

Although the detailed modeling the effect of dust scattering on polarimetric observations is not an easy task, it has been undertaken by some groups (eg. Natta & Whitney (2000); Isella & Natta (2005)) with a fair amount of success. These models use the theoretical dust scattering models to make predictions about the observed intensity of radiation when light is observed not only directly and partially obscured, but also seen scattered by the dusty disk surrounding the star. The models assume that some fraction f of the stellar surface is partially obscured by a screen of optical

depth τ_λ, so that the light received by the observer is given by:

$$F_{obs} = F_\star(1-\epsilon)[1 - f(1 - e^{-\tau_\lambda})] + F_{scat} \tag{1.11}$$

where $F_\star$ is the flux of the direct stellar light, F_{scat} is the flux of light scattered from the obscuring screen, and ϵ is the fraction of the stellar surface that is entirely blocked by the disk (Natta & Whitney 2000). Thus, $F_\star(1-\epsilon)$ represents the fraction of the stellar disk from which we receive any radiation at all, and of that fraction, some additional part ($f(1 - e^{-\tau_{lambda}}$) is partially obscured by dust. This equation illustrates well that there are two separate sources of radiation: the direct stellar radiation, in addition to the radiation scattered by a dusty disk. This two-component model is an important aspect of modeling the structures around young stars, and will be discussed in terms of specific observations in chapter 5. The overall polarization is modeled by considering the contribution of scattered light from different parts of the illuminated disk, which scatter light at slightly different position angles. In a symmetrical system, the position angles of the polarization tend to cancel, resulting in no detectable polarization. We return to these models in chapter 4.

In addition to modeling the problem from the angle of dust scattering models, observations relating the change in overall intensity of the stellar radiation to the observed polarization have resulted in testable relations that describe well the of some Herbig Ae/Be stars. For example, Grinin et al. (1991) consider the case where the observed polarization is due mainly to the contribution of scattered light from a disk. If the changes in the total polarization of the system are due solely to a change in the ratio of the amount of light being directly observed to the amount of light being scattered from the disk, then there should be a relationship between the varying magnitude of the star and the observed polarization. This relationship is described by the simple law (Grinin et al. 1991):

$$\vec{P}_{obs}(\Delta m) = \vec{P}_{is} + \vec{P}_{sc} 10^{0.4\Delta m} \tag{1.12}$$

where $P_{obs}(\Delta m)$ is the observed linear polarization of the star, P_{sc} is the polar-

ization of the star in its brightest state due to scattering, and P_{is} is the interstellar polarization. It has been observed that this relation is wavelength-dependent, so that an investigation of the changes in polarization as a function of wavelength may be useful in constraining the properties of the system.

Another potentially important mechanism for polarization is the absorption of light from aligned non-spherical dust grains. This mechanism induces polarization in the directly observed but obscured light, rather than in the light seen scattered from the disk. In order for this type of polarization to be significant, there would have to be a magnetic field present in the environment of the star that would align the dust grains. If present, the contribution of this polarization is added as a vector sum to the other components of polarization as follows (Grinin et al. 1988):

$$\vec{P}_{obs} = \vec{P}_{is} + \vec{P}_{sc} + \vec{P}_{al} \tag{1.13}$$

where again $\vec{P}_{is}$ is the interstellar polarization, $\vec{P}_{sc}$ is the polarization due to scattering off a disk, and $\vec{P}_{al}$ is the polarization due to aligned dust grains. If present, the contribution of this mechanism depends on the polarization properties (the optical dichroism) of the dust in circumstellar clouds, and it would also be dependent on the overall magnitude of the system (the star fades due to increasing dust obscuration, and the polarization increases due to the same effect). It is aligned dust grains that produce normal interstellar polarization, but the magnitude and direction of the interstellar polarization would not be expected to be the same as any polarization induced locally.

1.3 Summary

In this introduction, we have outlined the importance of astronomical polarimetry, and discussed some basic concepts that will appear in later chapters. We will return to the discussion of Herbig stars and the dusty disks that surround them in chapter 4. That discussion will be followed by a presentation of our simultaneous polarimetric

and photometric observations of these stars and an interpretation of the results, in chapter 5.

First, though, we discuss the instrument with which our observations were made: the PROMPT polarimeter. The instrumentation and design of the polarimeter are outlined in chapter 2, followed by a summary of the data acquisition, reduction, and analysis procedures, in chapter 3. The polarimeter and the data that it obtained over the course of 8 months from March-October 2007 are central to the goals of this thesis, and we will show that the successful design and assembly of the instrument, along with a successful observing campaign, have led us to new insights into the nature of the circumstellar environments of several young stars.

Chapter 2

The PROMPT Polarimeter

The PROMPT polarimeter was designed and built specifically for use on one of the PROMPT telescopes at the Cerro Tololo International Observatory (CTIO), in Chile. In this chapter, we present an overview of the PROMPT telescopes, followed by a detailed account of the polarimeter's instrumentation. We discuss initial specifications along with design challenges and how we dealt with them.

2.1 PROMPT

PROMPT is a group of 6 robotic telescopes designed to image gamma-ray burst (GRB) afterglows on a rapid time scale. Located at CTIO, PROMPT consists of six 0.41-meter Ritchy-Chretien telescopes mounted on rapidly slewing Paramount ME mounts. Each OTA and camera assembly is optimized for a particular wavelength range and function, including a NIR imager, two red-optimized imagers, a blue-optimized imager, a UV-optimized imager, and an optical polarimeter. Details regarding these components can be found in Reichart et al. (2005).

PROMPT's design allows for the simultaneous imaging of a source in multiple wave-bands. Typically, GRB afterglow observations are recorded in $u'g'r'R_ci'z'J$ and H bands, but $UVBRI$ filters are also available.

PROMPT observations are conducted remotely and often entirely robotically through the SkyNet software designed specifically for use with PROMPT. SkyNet receives sig-

Figure 2.1 The PROMPT P1 dome at CTIO.

nals from a satellite-based GRB network and slews the six telescopes to the potential afterglow location within seconds of notification. Non-GRB related observations may be conducted robotically via a queue system which prioritizes observations based on their location in the sky. Alternately, the PROMPT telescopes may be controlled remotely by a user directly inputting commands. The PROMPT dome housing the polarimeter (P1) is shown in figure 2.1.

2.2 The Polarimeter

The PROMPT polarimeter was originally designed with GRB observations in mind. However, it has a broad range of uses, particularly for targets of opportunity (TOOs) and long-term studies.

2.2.1 Motivation

The PROMPT polarimeter's primary function is to rabidly image GRB afterglows, and the idea of the PROMPT polarimeter was conceived of at a time when very few polarimetric observations of GRBs existed. The first measurement of any GRB polarization came from GRB 990510, when Covino et al. (1999) measured a polarization value of $1.7 \pm 0.2\%$, 18.5 hours after the beginning of the burst (Wijers et al. (1999) observed the same burst and measured a value of $1.6 \pm 0.2\%$ 20.64 hours after the burst). Rol et al. (2000) were the first to observe variability in the polarization of a GRB afterglow, measuring the variation of the polarization of GRB 990712 as 1.2% to 2.9% in the time period between 10.56 hours after the burst until 1.45 days afterwards. More significant levels of polarization were measured by Bersier et al. (2003), when they found a polarization level of 9.9%, 1.3 days after the first detection of GRB 020405. These measurements highlighted the need for the early-time polarimetry measurements of gamma-ray bursts, and it was under these circumstances that the initial plans to begin the design of the PROMPT polarimeter were laid out.

Soon after the decision was made to include a polarimeter as part of the PROMPT instrumentation, interest in GRB polarizations exploded, when in December 2002 the solar gamma-ray spacecraft RHESSI recorded a polarization value of $(80 \pm 20)\%$ for GRB 021206 (Coburn & Boggs 2003). Although this result was challenged (see, for example Rutledge & Fox (2004)), the idea that GRBs may exhibit an extremely high level of polarization at very early times began to be discussed. This high polarization could be explained if the jet that produces the GRB was magnetically, rather than hydrodynamically confined. In this scenario, the reverse shock, which is for the early optical emission, would propagate back through a highly ordered field, producing a high level of polarization at very early times (Granot & Königl 2003). Subsequent turbulence in the shock would result in a low level of polarization at later times, when the jet would lose its ordered quality.

The software development that will eventually allow the PROMPT polarimeter to respond on a time scale of seconds to GRB alerts is still ongoing, but the primary

motivation for the development of the instrument has not vanished, and there are still plans to use the polarimeter for rapid GRB afterglow follow-up. Unfortunately, the rate of GRB detections has been lower than expected prior to the launch of the SWIFT gamma-ray satellite, so the odds of catching a GRB that is both bright enough to image and above the horizon at the time of the burst have declined considerably. In the meantime, the polarimeter has been used successfully to image a variety of polarized sources, as will be discussed in chapter 4 and chapter 5.

As a final word about the primary motivation for the development of the PROMPT polarimeter, it should be noted that Mundell et al. (2007) have recorded polarization values of GRB 060418, beginning only 203 seconds after the initial burst. They found a polarization value $< 8\%$ during the fireball deceleration phase and the onset of the afterglow, effectively ruling out the presence of a large-scale ordered magnetic field, which models predict would result in observable polarization values of $> 10\%$ and up to 50% polarization (Rossi et al. 2004; Lazzati et al. 2004).

2.2.2 Design Specifications

The PROMPT polarimeter is a prototype astronomical polarimeter constructed using off-the shelf optics. Its design specifications outline the need for the polarimeter to be able to rapidly detect and follow up on GRB afterglows. We worked under stringent budget and schedule constraints to meet the following minimum design criteria:

- Simultaneously deliver separate images of a 5'x2.5' field with orthogonal linear polarization states onto a single CCD detector.
- Include an analyzer capable of rotating the polarization angle through a total of 67.5° (135° in Poincare space), in 22.5° steps.
- Be compact and light enough to attach to the PROMPT 16" telescopes without interfering with their operation.
- Pixel sampling of $< 0.5''$/pixel.

- Polychromatic spot sizes over a 400 nm range that degrade the image quality by no more than 0.05″ in the best seeing.

Some astronomical polarimeters already in use satisfy some of these criteria, but the instrument design has always involved some type of sacrifice. Some polarimeters still in use today are photoelectric polarimeters with a single aperture, unsuitable for imaging a large field of view or extended objects (eg. the polarimeter of Piirola (1975), still in use at the Crimean Astrophysical Observatory). The Durham polarimeter (Scarrott et al. 1983) produces a larger (9') field of view, but the image is interrupted by a series of parallel obscuring strips in the focal plane of the telescope to prevent image overlap, and it makes the image analysis difficult. Two other polarimeters, IMPOL and ARIES (Ramaprakash et al. 1998; Rautela et al. 2004) use a similar principle and suffer from the same difficulties. A design incorporating multiple wollaston prisms to eliminate the need for a half-wave plate has been put forth (Oliva 1997), but that would not help us to satisfy any of our criteria. Most other polarimeters either use two CCD cameras to simultaneously image the two orthogonal polarization states, or they image the two states separately.

2.2.3 The Basic Components of a Polarimeter

Any instrument that is to be used to measure polarization levels must consist, at the very least, of two basic components: an analyzer to rotate an incoming beam through a polarization angle of 67.5° in steps of 22.5°, and a polarizer to split the beam into two orthogonal polarization states. The rotating analyzer plays the same role as the filters used to describe the Stokes parameters in equation 1.9, with the advantage that instead of throwing away half the incoming light (as a polarizing filter does), the analyzer simply rotates the plane of polarization while maintaining the total flux of the radiation. The analyzer moves in steps of 22.5° in order to sample the polarization values at intervals of 45° in Stokes space. When used together, the analyzer and polarizer sample the differences in the illumination of the two orthogonal polarization

states at each of the four angles $(0°, 22.5°, 45°, 67.5°)$, thereby fully describing the Stokes parameters. This concept will be explored further in chapter 3.

The analyzer that was chosen for the PROMPT polarimeter is a Fresnel rhomb (from Karl Lambrecht Corporation, part # MFRC2-20-580, see figure 2.2). The rhomb operates on the principle of total internal reflection – this reflection produces a phase delay between the -p (parallel to the plane of incidence) and -s (perpendicular to the plane of incidence) vibration components of the incoming light wave. The Fresnel rhomb is a half-wave retarder, and as such, it rotates the angle of polarization by 90°. The rhomb is made from BK7, and consists of two prisms held in place with a mount and cemented together. The Fresnel rhomb is treated with an anti-reflection coating to optimize its performance. Complete technical specifications for the rhomb are given in table 2.1. The principal reason that a Fresnel rhomb was chosen over another type of half-wave retarder was the large wavelength range under which the rhomb can operate (330-1000 nm). The main disadvantages of using a Fresnel rhomb rather than an achromatic half-wave plate are the larger weight and length of the rhomb compared to the half-wave plate.

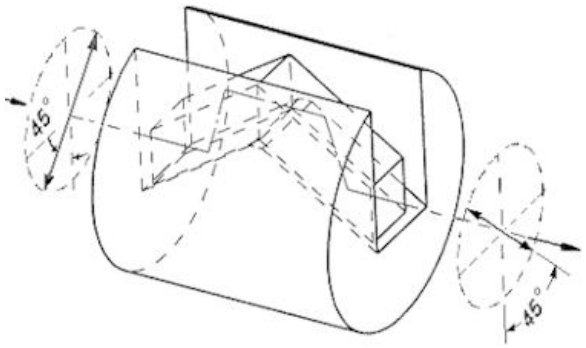

Figure 2.2 The Fresnel rhomb used in the PROMPT polarimeter. The rhomb is a half-wave retarder that polarizes under the principle of total internal reflection.

The Fresnel rhomb is mounted on a Newport goniometric cradle (part number BG80-0.1), which is able to rotate the rhomb through 90°. By taking images with the rhomb oriented at different positions, the Stokes parameters Q and U can be measured.

Parameter	Value
Material	BK7
Wavelength Optimization	580nm
Contact	Cemented
Reflection Coating	HEAR 400-700nm
Reflectivity per Surface	0.3% average
Surface Quality	40-20 scratch dig
Clear Aperture Diameter	20mm
±2% Retardation Error Range	330 - 1000nm
Mount Outside Diameter	4.375 inches
Mount Length	4.250 inches

Table 2.1 Technical Specifications for the Fresnel Rhomb.

The goniometric cradle has a resolution of 0.001° and a typical on-axis accuracy of 0.05°. The cradle is rotated via a Silvermax motor (part number QCT-17H-1-E-01), under the operation of a specialized quicksilver software routine (www.qcontrol.com).

The polarizer for the PROMPT polarimeter is a wollaston prism (from Karl Lambrecht Corporation, part number MW2A-20-5; see figure 2.3). The wollaston is made from two pieces of calcite fused together in such a way that a beam entering the prism will be split into two components with orthogonal polarizations and trajectories separated by 5°. These two orthogonal polarization states are then be imaged simultaneously. Like the Fresnel rhomb, the wollaston prism is treated with anti-reflection coating and optimized for a large wavelength range. Complete technical specifications are listed in table 2.2

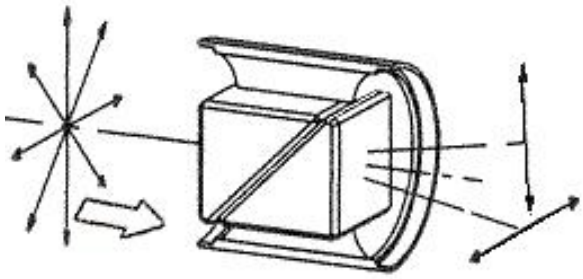

Figure 2.3 The Wollaston prism, a calcite beam-splitter that separates the two polarization states of the incoming beam.

Parameter	Value
Material	Grade A Calcite
Wavelength Optimization	350-2300nm
Reflection Coating	HEAR 400-700nm
Surface Quality	40-20 scratch dig
Clear Aperture	20mm
Angular Separation @ 600nm	5°
Asymmetry @ 600nm	$(\frac{1}{6})^\circ$
Mount Outside Diameter	1.373 inches
Mount Length	0.750 inches

Table 2.2 Technical Specifications for the Wollaston prism.

2.2.4 Additional Design Components

In addition to the analyzer and the polarizer, there were several additional components that were added to the polarimeter in order to make it function according to the design criteria.

The first component of the polarimeter is a dual filter wheel, with polarizing filters mounted in the first wheel, followed by $UBVR$ filters in the second. The filter wheel is made by Astronomical Consultants & Equipment Inc (ACE). It interacts with the imaging software MaxIm DL, and is also programmable for custom movements.

The polarizing filters in the first wheel are Meadowlark precision linear polarizers. These three filters in combination cover a wavelength range of $330 - 1800$ nm, and are used for calibration purposes to ensure that the polarimeter is making accurate measurements of incoming polarized light. The second wheel holds Bessel $UBVR$ filters, from Omega Optical Corp.

The Fresnel rhomb mounted on the goniometer is located directly behind the filter wheel. The image plane falls very close to the output of the rhomb, where a mask is placed to reduce the field to $\frac{1}{2}$ the CCD area (to allow two side-by-side images to fit on the CCD). The mask is mounted on a pair of micro positioning stages (Edmund Optics part #38-526) that allow the mask to be moved in the x- and y-directions, ensuring that the resulting images will fall on the CCD in the appropriate spot.

Following the mask is a 1:1 re-imaging system built from a matched pair of off-the-shelf achromats (Edmund Optics part #R32-323). The collimated beam is split into two orthogonal polarization states by the Wollaston prism before the pupil. The final component of the polarimeter is the CCD camera (Apogee U47+), which images the two orthogonal beams simultaneously.

The optical layout behind the rhomb is shown in figure 2.4, with rays shown for only one of the two polarization states. The Wollaston prism introduces severe chromatic effects, as shown in the spot diagram in figure 2.5, so this layout does not meet the image quality specifications.

It proved possible to counter the chromatic effects using a rooftop shaped BK7

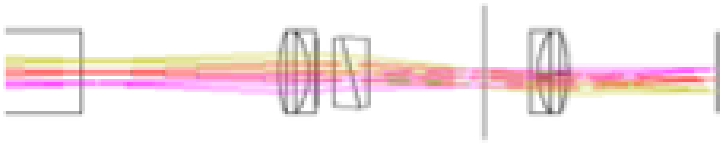

Figure 2.4 The first optical layout for the PROMPT polarimeter.

prism. This prism was assembled by aligning two halves of a 14.85° wedge prism (Edmund Optics part #R45-562). One pupil image falls on each side of the prism, so that the final images are reversed from the previous layout (see figure 2.6).

Unfortunately, it is not possible to get the two orthogonally polarized pupils separated far enough to avoid mixing across the center of this element. By stopping the entrance pupil of the telescope to 11", it is possible to get good channel separation and to meet the image quality specifications, as seen by the spot diagram in figure 2.7. The downside to this solution is that the total area of the mirror is reduced by 53%, reducing the polarimeter's capacity to image faint sources. The solution has, however, been implemented, allowing the polarimeter to operate in a "masked" mode, with reduced light-gathering capability but increased image quality. The mask must be attached or removed on-site at CTIO, so switching from masked to unmasked mode is not possible when operating the system entirely remotely.

When operating the polarimeter in the "unmasked" mode, there is a strip of the CCD that should not be used for imaging, since it is contaminated with light from the orthogonal state. The "unusable" strip is the right-most third of the left-sided

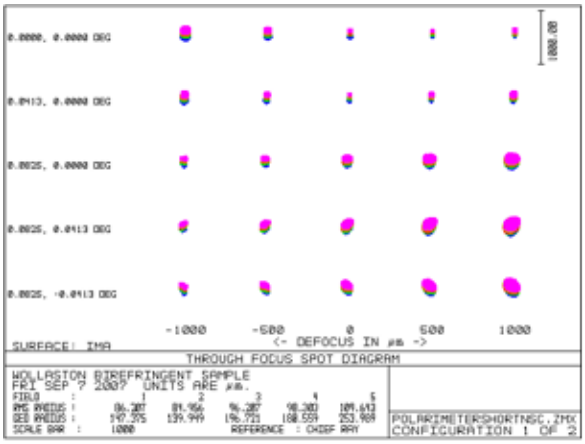

Figure 2.5 The spot diagram of the output of the first optical layout for the polarimeter.

image, and the left-most third of the right-sided image. Since the left-and right-side of the CCD are identical, this effectively leaves only the center third of the image as usable. However, since the telescope mirror is not obscured, when the polarimeter is operating in this mode it can observe fainter sources.

2.2.5 The Completed Instrument

The PROMPT polarimeter is shown, fully assembled and mounted on the PROMPT P1 telescope, in figure 2.8. In addition to the components already discussed, the polarimeter is stabilized by a custom-made aluminum support arm. This support arm fits into the dovetail joint on the "Versa-Plate" supplied with the Paramount ME mount, and it prevents excessive flexure of the instrument. The total weight of the polarimeter + OTA does not exceed the limits of what the Paramount can handle (150 lbs). A detailed description of the mechanical and electrical assembly of the polarimeter can be found in appendix B.

2.3 Initial Results

The PROMPT polarimeter was initially tested at the Morehead observatory in Chapel Hill (mounted on a small telescope riding piggyback on the larger, permanent

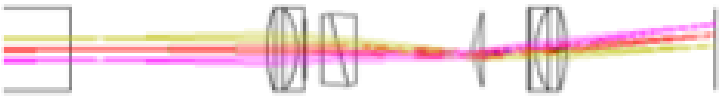

Figure 2.6 The second optical layout of the polarimeter, showing the effect of the added rooftop prism.

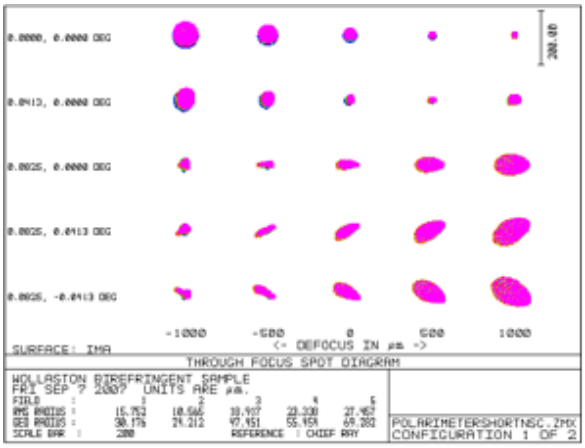

Figure 2.7 The spot diagram of the output of the second optical layout. Note the difference in scale from layout 1.

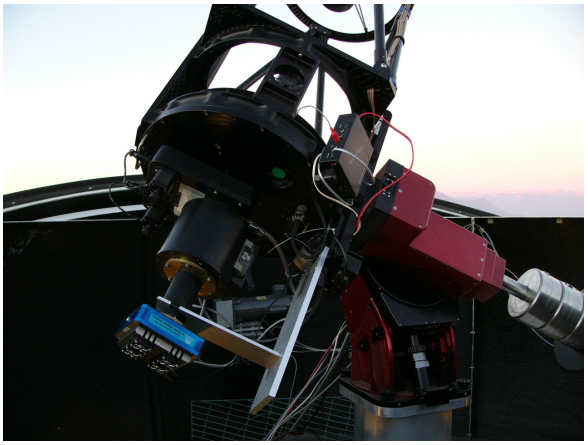

Figure 2.8 The PROMPT Polarimeter, installed on the P1 telescope on Cerro Tololo.

24-inch telescope). Following promising initial results it was successfully installed at its permanent home on the PROMPT P1 telescope at CTIO in October 2006. This section outlines some of the initial observations and instrument calibrations performed, including observations of polarized standard stars and null sources.

2.3.1 Polarized Standards

In the time period between October 2006 and June 2007, polarized standard stars were observed repeatedly to watch for any trends in polarization. Polarized standards typically have polarization values between $1\% - 7\%$, and a wide range of θ values. The polarization of standard stars is generally caused by interstellar sources, and is therefore unlikely to change significantly. The most important role of the standard stars is to calibrate the position angle, θ. Our standard star observations are detailed in table 2.3.1 and illustrated in figure 2.10 and figure 2.11. From these observations we have calculated a position angle offset of $+11.0^\circ \pm 2.5^\circ$. This offset has been added to all future observations.

StarID	F/O	$\%P_e$	σ_{P_e}	$\%P_m$	σ_{P_m}	θ_e	σ_{θ_e}	θ_m	σ_{θ_m}
HD43384	O, X	2.75	0.00	2.95	0.25	170.5	0.7	157.5	1.6
HD160529	V	7.31	0.04	7.74	0.34	20.1	0.1	8.2	1.5
HD154445	V	3.74	0.01	3.36	1.00	90.1	0.7	77.7	2.1
HD245310	V	3.91	0.00	4.78	0.47	146.0	1.0	136.6	1.6
HD245310	O	3.91	0.00	3.84	0.23	146.0	1.0	135.1	1.2
HD245310	V	3.91	0.00	3.71	0.23	146.0	1.0	138.8	1.2
HD127769	V	1.49	0.02	1.39	0.25	54.0	0.4	40.9	1.4
HD245310	V	3.91	0.00	3.97	0.23	146.0	1.0	135.9	1.3
HD245310	V	3.91	0.00	4.09	0.17	146.0	1.0	137.2	1.0
HD43384	V	2.75	0.00	2.19	0.47	170.5	0.7	159.4	1.7
HD245310	V	3.91	0.00	4.14	0.24	146.0	1.0	137.5	1.2
HD154445	B	3.74	0.01	2.87	0.66	90.1	0.7	75.8	2.0
HD43384	V	2.75	0.00	2.36	0.29	170.5	0.7	161.4	1.4
HD43384	V	2.75	0.00	3.12	0.29	170.5	0.7	164.9	1.4
HD245310	V	3.91	0.00	4.24	0.11	146.0	1.0	137.6	1.2
HD127769	V	1.49	0.02	1.31	0.21	54.0	0.4	40.3	1.2
HD245310	V	3.91	0.00	4.23	0.31	146.0	1.0	137.7	1.5
HD127769	V	1.49	0.02	1.34	0.21	54.0	0.4	38.0	1.4
HD142863	V	1.89	0.06	1.86	0.17	83.7	1.0	74.0	1.1
HD147084	V	4.18	0.02	3.81	0.26	32.0	0.1	16.9	1.6
HD245310	V	3.91	0.00	4.23	0.27	146.0	1.0	137.2	1.8
HD127769	V	1.49	0.02	1.37	0.12	54.0	0.4	40.1	1.0
HD142863	V	1.89	0.06	1.84	0.14	83.7	1.0	75.7	1.1
HD147084	V	4.18	0.02	3.10	0.27	32.0	0.1	18.0	1.4
HD160529	V	7.31	0.04	7.35	2.25	20.1	0.1	8.4	2.3
HD160529	R	7.31	0.04	7.00	2.23	20.1	0.1	6.8	2.3
HD162061	V	3.18	0.14	3.18	0.20	65.8	1.3	56.2	1.4
HD181474	V	1.15	0.02	0.97	0.20	74.6	0.4	63.6	1.7
HD185198	V	1.68	0.04	1.33	0.20	76.0	0.6	65.3	1.2
HD185198	V	1.68	0.04	1.40	0.19	76.0	0.6	66.1	1.2

Table 2.3 Results of the observations of standard stars. Some stars were observed multiple times. Column 1 is the star identification, column 2 is the filter and orientation of the polarimeter (an X designation means that the instrument was rotated 90° with respect to the telescope at the time of observation), column 3 is the expected %Polarization, column 4 is the error in the expected %Polarization, column 5 is the measured %Polarization, column 6 is the error in the measured %Polarization, column 7 is the expected position angle, column 8 is the error in the expected position angle, column 9 is the measured position angle, and column 10 is the error in the measured position angle. The calculated position angle offset from these measurements is $11.0° \pm 2.5°$.

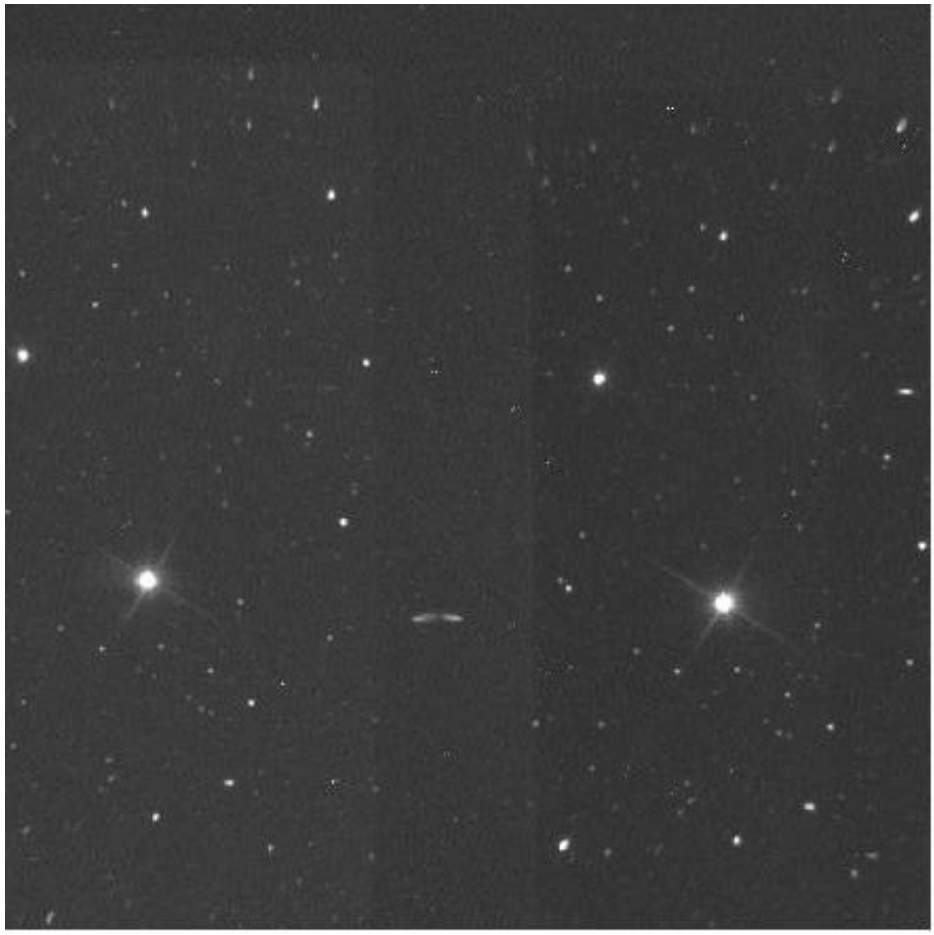

Figure 2.9 An example of the images obtained with the PROMPT polarimeter. This is HD98922.

2.3.2 Null Standards

During the same period of time that the polarized standards were being observed, many observations of null sources were also made. Null standards are stars that display very little ($< 0.1\%$) polarization. They are difficult to measure accurately, but substantial polarization values recorded consistently when observing null sources can indicate a problem in the instrumentation. As can be seen in table 2.3.2 and figure 2.12, there is an instrumental polarization of about 0.4% present.

StarID	F/O	$\%P_e$	$\%P_o$	σ_{P_o}
HD20630	O	0.006	0.603	0.5
HD222368	O	0.025	0.553	0.3
HD222368	O, X	0.025	0.812	0.5
HD45737	O, X	0.031	0.878	0.8
HD56986	V	0.001	1.017	1.1
HD64299	V	0.151	0.100	0.3
HD98161	V	0.017	0.476	0.5
HD117176	V	0.004	0.064	0.4
HD98161	V	0.017	0.208	0.6
HD98161	B	0.017	0.355	0.5
HD94851	V	0.057	0.186	0.4
HD94851	R	0.057	0.099	0.2
HD176425	V	0.02	0.385	1.0
HD176425	R	0.02	0.327	0.7
HD48737	V	0.031	0.732	0.6
HD98161	V	0.017	0.114	0.2
HD117176	V	0.004	0.512	0.3
HD48737	V	0.031	0.614	0.3

Table 2.4 Null Standard data collected from the PROMPT polarimeter for calibration purposes. Some stars were observed more than once. Column 1 is the star's identification, column 2 indicates the filter used and the orientation of the polarimeter at the time of observation (an "X" means that the polarimeter was rotated 90° with respect to the rest of the instrument at the time of the observation), column 3 is the expected polarization value, column 4 is the measured polarization, and column 5 is the error in the measured polarization.

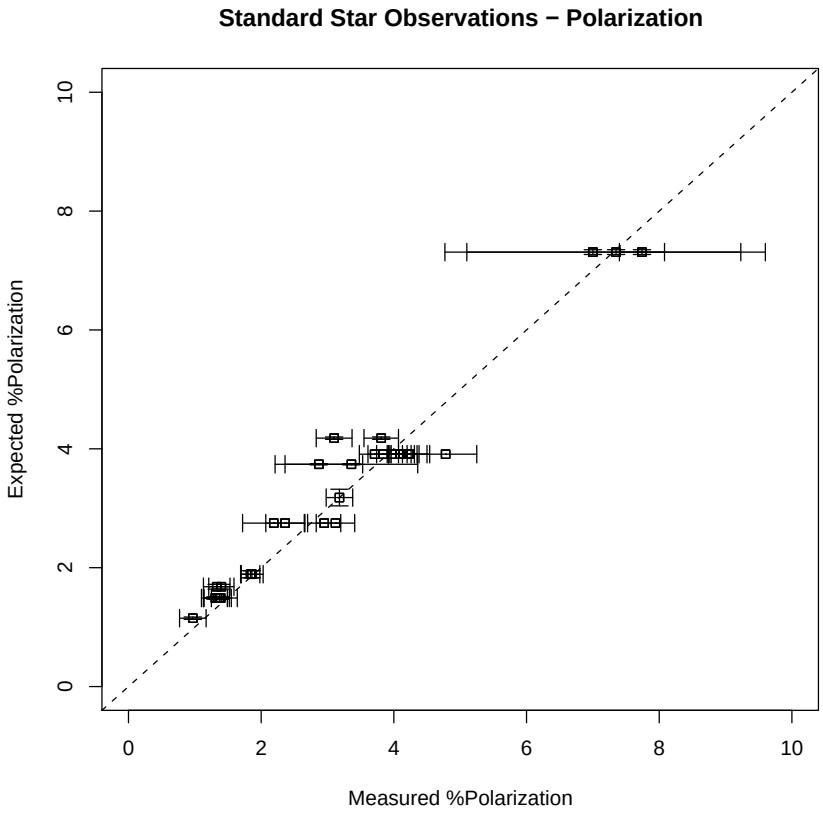

Figure 2.10 Measured vs. Expected values of the polarization values for the standard star observations listed in table 2.3.1. The dashed line indicates $\%P_e = \%P_m$.

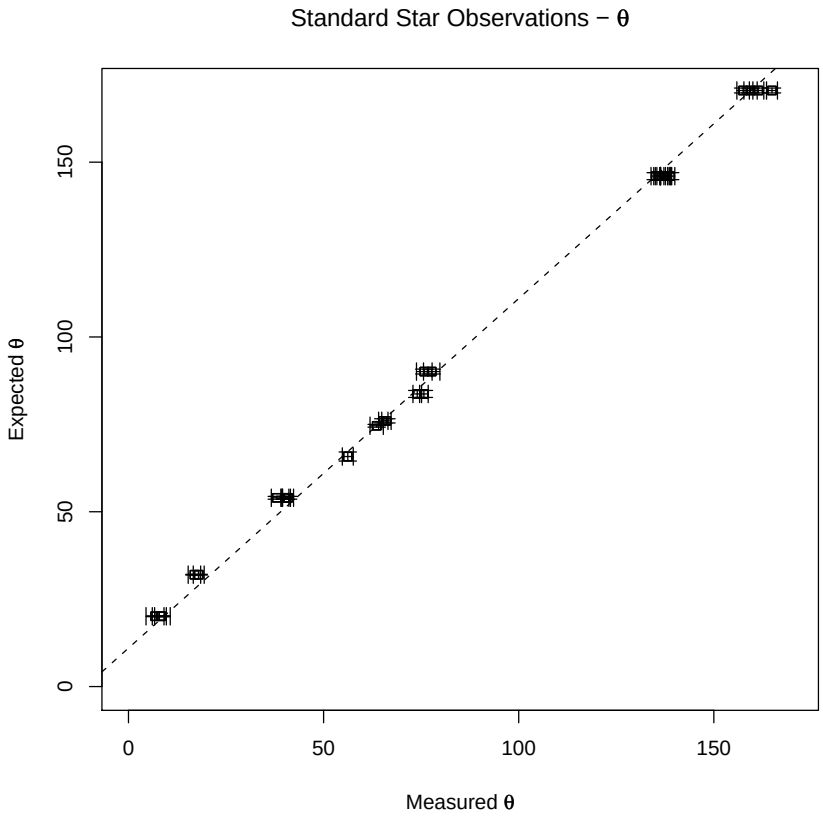

Figure 2.11 Measured vs. Expected values of the θ values for the standard star observations listed in table 2.3.1. The dashed line indicates $\theta_e = \theta_m + 11.0$.

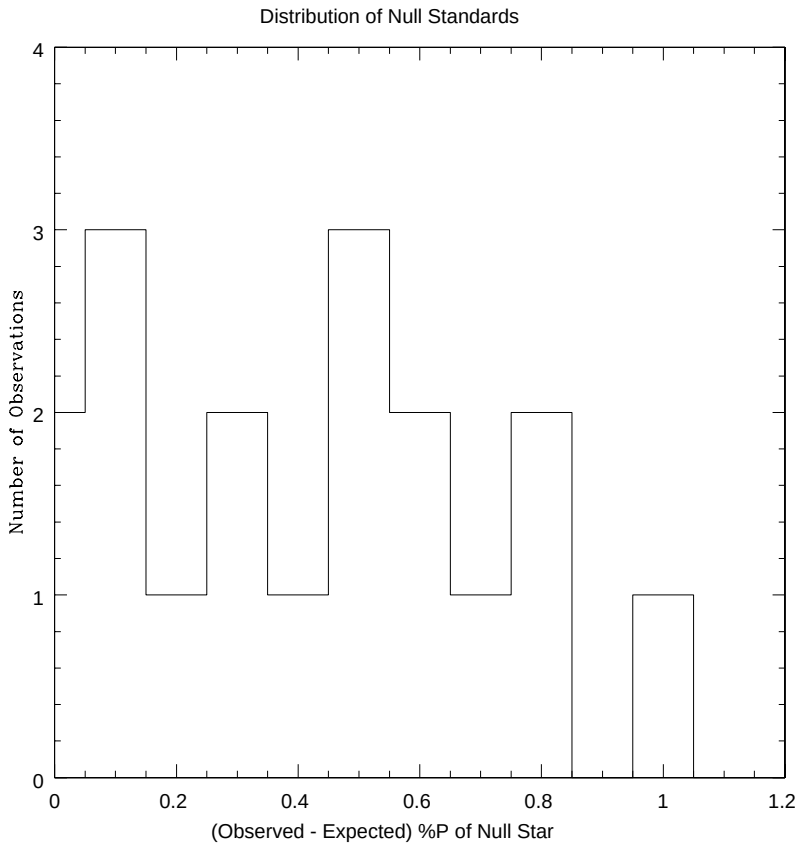

Figure 2.12 A histogram of the recorded polarization of the null stars that were observed. The average polarization is 0.4%.

Chapter 3

Polarimetry in Practice

Having a theoretical understanding of the principals of polarimetry is a necessary but not sufficient requirement for being able to collect and interpret polarimetric data. In this chapter we outline some of the essential observing and reduction procedures that build a foundation for successful data analysis. These procedures have been implemented with the specific needs of the PROMPT polarimeter in mind.

3.1 Polarimetry Observing Procedures

Polarimetric data represents a different kind of tool than the ones with which most astronomers are accustomed to using. Although there are many aspects of observing that are no different from normal image acquisition, there are a few important details that must not be neglected. Those details are expanded upon in this section.

3.1.1 Data Acquisition

The PROMPT polarimeter is an imaging polarimeter, and as such data acquisition is relatively straightforward. If the images are being collected in an interactive mode (ie. not robotically), then a visual inspection of the images may be performed as they are acquired. Here, the same standards that apply to any imaging camera should be applied, namely that the source be in focus and display a favorable signal-to-noise

ratio. The centering of the source is also of particular importance when using the PROMPT polarimeter. As is discussed in chapter 2, the polarimeter may be operated in either of two modes - masked or unmasked. When the polarimeter is being operated in unmasked mode, it is essential the the source be centered in each of the dual images in the horizontal sense. The centering will prevent the source from being contaminated by overlapping light from the opposite side. When operating in masked mode, the overlapping states are not as problematic, but it is generally good practise to center the source nonetheless to maintain optimal image quality.

In addition to any general concerns that are issues during any kind of image acquisition, there are several polarimeter-specific concerns. The most obvious of these concerns the rotation of the Fresnel rhomb that serves as a half-wave plate for the polarimeter. One "set" of images consists of 4 separate images with the rhomb oriented at 4 different values. The first two orientations, at 0° and 45°, define the Q Stokes' parameter, while the second two orientations, at 22.5° and 67.5°, define the U Stokes' parameter. It is important to measure the values that define each Stokes parameter together, so the set should be imaged in the order 0°, 45°, 22.5°, 67.5°. The exposure time should be constant for a set. Note also that these values assume a rotation range of $0-90°$; since the goniometer on the polarimeter rotates from $-45°$ to 45° the actual values that are input into the goniometer are $-34°$, $+11°$, $-11.5°$, and $+33.5^{circ}$.

Finally, there are two simple rules to follow to avoid observing at times when there is a significant amount of sky polarization. Don't observe when the moon is full, and always begin after and quit before astronomical twilight.

3.1.2 Standards and Calibration Stars

Doing polarimetry requires observing polarimetric and null standard stars throughout an observing run, in addition to the usual photometric standards. Luckily, many of the polarimetric and null standards can be used as photometric standards as well.

Lists of polarized standards have been compiled by several authors (see, for example Serkowski et al. (1975) and Hsu & Breger (1982)). Polarization values of the

standard stars range from around 1% to close to 9%, and have a wide range of θ values. Observed % polarization should be within 10% of the standard value, and in most cases there will be an adjustment that must be made to the observed θ value in order to bring the observation in line with the standard star. For this reason, when observing polarimetric standards, stars with a spread of θ values from $0 - 180^{\circ}$ should be chosen if at all possible. The additive θ value should not change over the course of an observing run, but should be re-calculated in case of any physical changes made to the polarimeter.

Null standards are stars that exhibit no polarization ($\%P$ is zero and θ is undefined). They are notoriously hard to measure accurately, but observations of these stars can be illuminating nonetheless. Since polarization is an intrinsically positive value, there is almost always a measurement bias resulting in observed values that are higher than expected. Consistent $\%P$ observations over 1% should be considered suspicious, as should any observation with a definable θ value.

3.1.3 The Effects of Sky Polarization

The polarization of the sky is a very real effect that can introduce significant error into a set of observations if not properly taken into account. Sky polarization is primarily casued by the reflection of moonlight (or sunlight, during twilight hours) by the atmosphere and by high-altitude cloud cover, and can reach values of up to 15% on nights with a full moon.

The IRAF aperture photometry routine apphot calculates total flux values based on the formula Flux = sum - area*msky, where sum is the total number of counts in the aperture including sky, area is the area of the aperture in square pixels, and msky is the best estimate of the sky value per pixel. If sky polarization is appreciable, then some frames will have a higher sky value than other frames. That higher sky value being subtracted from the total number of counts (the "sum" value in IRAF), can lead to an artificially low measured flux value in those frames.

An estimate of the sky polarization can be made by comparing a region of blank

sky in each of the four frames used for polarization measurements. The sky variations should be small in comparison to the total flux values recorded for the source in the 4 frames. When observing bright objects, the sky value is generally 1% or less of the flux value of the object under observation, so that any sky fluctuation will be well within the statistical error bars for that observation. Sky polarization is more of a concern when observing faint objects with long exposure times, as in these cases the sky values can be significant when compared to the source flux.

The best way to avoid introducing errors due to sky polarization is to avoid observing when the moon is up, or to limit observations to regions of the sky that are not close to the moon (avoiding twilight observations is also recommended).

3.1.4 Re-Calibrating After Altering the Instrument

The PROMPT polarimeter is designed to be mounted permanently on one of the PROMPT telescopes, and as such, once the initial calibration is completed there should be no reason to complete another full-scale calibration, provided that measurements of standard and null sources remain within reasonable limits. However, if the polarimeter is removed for maintenance or if any of the components on it are changed (camera, filter, OTA), then the instrument should be re-calibrated. The following steps outline the procedure for calibrating the instrument. Each step should be repeated in each filter that will be used with the instrument - it is unlikely, but not unheard of, that filters will cause some degree of polarization. The goal of this procedure is to determine if there is any instrumental polarization and to characterize the polarization angle offset.

The first step is to image any bright star with a polarizing filter in place. The PROMPT polarimeter is equipped with a dual filter wheel specifically for this purpose. This is the easiest measurement that the instrument can make, and should return a value very close to 100% polarization (the value of the angle, θ, is not important). This measurement should be repeated at least twice, on 2 different stars, and can be completed during twilight hours (the remaining steps require complete darkness).

The second step involves imaging at least 3 polarized standards. The $\%P$ values should be within 10% of the standard values. If there is a θ offset, it should be consistent from star to star.

The final step is imaging at least 3 null standards. The null stars should be imaged initially with the polarimeter in its usual position, then imaged a second time with the polarimeter rotated by 90° with respect to the telescope. If there is a significant change in the measured values when the polarimeter is rotated, it can indicate that there is polarization being introduced by a component of the telescope (the mirror, filters, and even windows on the camera or cooling dewars can be responsable for this). If present, this polarization should be taken into account in all future measurements.

3.2 Polarimetry Reduction Procedures

The polarimetry reduction procedures have been split into two sections. The first section is a general treatment of the reduction problem, while the second section is more specific to the PROMPT polarimeter.

3.2.1 Data Reduction - General Treatment

Consider the most generalized form of polarized radiation that we may be able to imagine: partially elliptically polarized radiation propagating along the z-axis. The electric vector of this radiation can be separated into x and y components, in the same way as was done in chapter 1, equation 1.6 with generalized coordinates:

$$\begin{aligned} E_x &= A_1 cos(\omega t) \\ E_y &= A_2 cos(\omega t + \delta). \end{aligned} \tag{3.1}$$

Here ω is the frequency of the radiation, A_1 and A_2 are the amplitudes, and δ is the phase difference between the x and y components. It can be shown that (Chandrasekhar 1960):

$$a = \frac{(A_1^2 + A_2^2)^{\frac{1}{2}}}{1 + \tan^2\left(\frac{1}{2}\sin^{-1}(\frac{2A_1A_2\sin\delta}{A_1^2+A_2^2})\right)} \tag{3.2}$$

$$b = a\tan\left(\frac{1}{3}\sin^{-1}\left(\frac{2A_1A_2\sin\delta}{A_1^2+A_2^2}\right)\right) \tag{3.3}$$

$$a^2 + b^2 = A_1^2 + A_1^2 \tag{3.4}$$

$$\theta = \frac{1}{2}\tan^{-1}\left(\frac{2A_1A_2\cos\delta}{A_1^2 - A_1^2}\right) \tag{3.5}$$

where a and b are the semi-major and semi-minor axes of the ellipse, respectively, and θ is the angle between the x-axis and the major axis of the ellipse. The linear Stokes parameters are then defined by the following equations:

$$Q = A_1^2 - A_2^2 = \frac{a^2 - b^2}{a^2 + b^2}(\cos 2\theta)(IP) \tag{3.6}$$

$$U = 2A_1A_2\cos\delta = \frac{a^2 - b^2}{a^2 + b^2}(\sin 2\theta)(IP) \tag{3.7}$$

where I is the beam intensity and P is the fractional linear polarization. For linearly polarized light, $\delta = 180^\circ$ and $b = 0$ so:

$$Q = A_1^2 - A_2^2 = (\cos 2\theta)(IP) \tag{3.8}$$

$$U = 2A_1A_2\cos\delta = (\sin 2\theta)(IP) \tag{3.9}$$

In our data reduction procedures, we use the normalized Stokes' parameters:

$$q = \frac{Q}{I} = \cos 2\theta \qquad u = \frac{U}{I} = \sin 2\theta \tag{3.10}$$

Finally, the relevant astronomical quantities, P, the fractional linear polarization, and θ, the position angle, are given by the following formulae:

$$P = \sqrt{Q^2 + U^2}, \qquad \theta = (\frac{1}{2})\tan^{-1}\frac{U}{Q} \tag{3.11}$$

The position angle θ is defined to be the angle between the semi-major axis and the x-axis, when the x-axis is aligned north-south in the plane of the sky.

3.2.2 PROMPT Polarimeter Data Reduction

The PROMPT polarimeter measures three of the four Stokes' parameters - the total intensity, I, and the linear polarization parameters Q and U. The fourth Stokes' parameter, V, is used in the measurement of circular polarization.

There are several assumptions that are implicit in these data reduction procedures, the first of which are that the instrumental characteristics are constant with time. This assumption is checked by observing null standards (stars with known small intrinsic polarizations) several times during an observing run. Another assumption is that the instrumental polarization is negligible. We have shown this to be true for the PROMPT polarimeter, measuring an instrumental polarization of 0.4%, which is negligible for the results discussed in this thesis. We have not corrected for this instrumental effect in our results, but for an instrument that shows a significant amount, the instrumental polarization is subtracted from the Q and U values of the object before any other corrections are applied.

Two more assumptions that we make throughout this analysis involve the properties of the fresnel rhomb. We first assume that the fast axis of the rhomb is a slowly varying function of wavelength. This means that a single value for the position angle correction is valid. Our second assumption is that there is very little circular polarization mixed into the linear polarization measurements. This depends on the retardance of the rhomb being accurately half-wave at all wavelengths. The theoritical retardation of the fresnel rhomb is shown in figure 3.1. Its retardation value is 0.5 ± 0.01 over a range of wavelengths from 330 to 1000 nm. The additional observation that most astronomical sources show neglible circular polarization in the first place makes the assumption of negligible mixing of circular and linear polarization a valid one.

Polarimeter calibration data should be taken during each observing run. This includes the standard CCD reduction calibration frames - bias frames, dark exposures and flat fields - as well as data to check the efficiency of the polarimeter, calibrate the position angle and flux calibrate the data. In polarimetry measurements the flat field serves a dual purpose. It removes any changes in pixel-to-pixel sensitivity, but it also

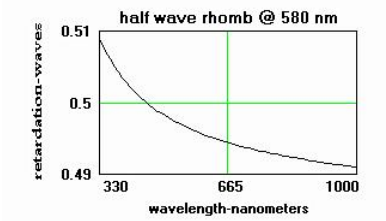

Figure 3.1 The retardance of the fresnel rhomb in the wavelength range 330-1000 nm. The deviation from half-wave is no more than 2% in this range.

removes efficiency differences in the system below the retarder, including the relative efficiencies of the two beams through the beamsplitter. The position angle correction is obtained by observing polarized standard stars. Null standards are also observed to check the instrumental polarization. Flux standards may also be observed to flux calibrate the images.

The first reduction tasks are all done using IRAF image processing packages. Bias, dark, and flat filed corrections are all applied, follwed by image alignment and combination done by set.

Two sets of four images each (i.e. eight images total) are used to determine a given Stokes' parameter. We will call these sets A and B. One set of four images (A_1, A_2, A_3, A_4) is taken at an initial position of the fresnel rhomb, and the second set of four images (B_1, B_2, B_3, B_4) is taken at a position 45° from the original. The four images in each set should be aligned and combined to produce one single, combined image (the images A and B). Since each image displays two identical pictures of the source being analyzed, we will use r and l to refer to the left- and right-hand pictures respectively. The four images in determining a given Stokes parameter are then A_r, A_l, B_r and B_l. The total intensity of the source being analyzed is the sum of the intensities on the left- and right-hand side of the image:

$$I_A = I_{A_r} + I_{A_l} \tag{3.12}$$

$$I_B = I_{B_r} + I_{B_l} \tag{3.13}$$

In theory, these intensities should be the same, but due to atmospheric transmission changes they are often not.

Following the methods of Trammell (1994), we will follow the beam through its optical path, noting the polarization state of the beam both above and below the beamsplitter (the wollaston prism). Above the beamsplitter, the fraction of light in each of the two polarization states is designated as p_0 and p_{90}, where $p_0 + p_{90} = 1$ and $p_0 = p_{90} = 0.5$ for unpolarized light. Below the beamsplitter the two polarization senses are split into two beams, and those beams will be considered separately. The detector quantum efficiencies may be represented by $\eta_{0_{jk}}$ and $\eta_{90_{jk}}$, where the subscripts are used to allow for the fact that detector efficiency varies from pixel to pixel. The throughput of the instrument for the two polarization senses will be denoted f_0 and f_{90}. We can then write the measured values of the four images as:

$$A_r = I_A p_0 f_0 \eta_{0_{jk}} \tag{3.14}$$

$$A_l = I_A p_{90} f_{90} \eta_{90_{jk}} \tag{3.15}$$

$$B_r = I_B p_{90} f_{90} \eta_{90_{jk}} \tag{3.16}$$

$$B_l = I_B p_0 f_0 \eta_{0_{jk}} \tag{3.17}$$

During the first step in the reduction, the bias level is subtracted and the images are divided by a flat field exposure. The flat field removes the pixel-to-pixel variations η_{jk} and the beam throughput corrections f_0 and f_{90}. However, flat fields are taken using partially polarized light sources such as the twilight sky or light reflected from the inside of a dome. This introduces another factor p' which represents the polarization of the flat field source and enters as a multiplicative factor. Thus, we have:

$$A_r = \frac{I_A p_0}{p'_0} \tag{3.18}$$

$$A_l = \frac{I_A p_{90}}{p'_{90}} \tag{3.19}$$

$$B_r = \frac{I_B p_{90}}{p'_{90}} \tag{3.20}$$

$$B_l = \frac{I_B p_0}{p'_0} \tag{3.21}$$

The normalized Stokes parameter is calculated as:

$$q = \frac{Q}{I} = \frac{A_r - B_r}{A_r + B_r} \tag{3.22}$$

so that the p' factors cancel out and do not affect the final result. However, the intensities I_A and I_B do not cancel out of this equation. It is therefore necessary to apply an intensity ratio correction (balance factor), $\omega = \frac{I_A}{I_B}$ to the Stokes parameter. Once ω has been calculated, the Stokes parameter q can be calculated in two different ways:

$$q_r = \frac{A_r - \omega B_r}{A_r + \omega B_r} \qquad q_l = \frac{\omega B_l - A_l}{\omega B_l + A_l} \tag{3.23}$$

The average q value is given as:

$$q_{ave} = \frac{q_r + q_l}{2} \tag{3.24}$$

The quantity q_{ave} has a slightly smaller pixel-to-pixel noise than q_r and q_l.

This process is repeated with the remaining two sets of images (C and D) to calculate the Stokes' U parameter.

This method is outlined again in appendix A where the equations are written out explicitly in terms of the actual values being measured in the IRAF aperture photometry package.

3.2.3 Error Analysis

As was alluded to briefly in section 3.2.2, a considerable source of error in the polarimetry reduction process is the flatfield, since a flatfield image is almost always polarized, being acquired either from the twilight sky or from an illuminated screen inside a dome. The error analysis takes this into account. This procedure assumes that the CCD parameters gain and readnoise are known, and that the noise in the images arises only from readout noise and counting statistics.

For a single pixel in an image A, the error associated with the measurement of the total flux is given by:

$$\sigma^2(A) = \frac{S}{F^2} + \frac{r^2}{F^2} + \frac{1}{N_B}\frac{B}{F^2} \tag{3.25}$$

where r is the readout noise in electrons, S is the number of counts from the object in the pixel, and F is the number of counts in the flat field for the pixel. B is the total number of background counts determined from a number of pixels in the image (the sky value), and N_B is the number of pixels used to determine the background level. The σ value should be computed for each image individually (A_r, A_l, B_r and B_l), and the balance factor ω should be calculated. Then the error in the Stokes parameter, $\sigma^2(q)$, can be calculated:

$$\sigma_r^2(q_r) = \frac{4\omega^2}{(A+\omega B)^4}(A^2\sigma_r^2(B) + B^2\sigma_r^2(A)). \tag{3.26}$$

The error associated with q_l is carried out in the same way. We may also calculate:

$$\sigma^2(< q >) = \frac{1}{4}(\omega_r^2 + \omega_l^2). \tag{3.27}$$

The process is repeated with the next two sets of images that determine the Stokes u parameter.

3.3 Photometry with the Polarimeter

As the PROMPT polarimeter is an imaging polarimeter, photometry is relatively straightforward. The only way in which the photometry procedure varies from that of a normal imaging system is that the flux values from each side of the image should be added together before the magnitude is calculated. So for image A, $A = A_r + A_l$ is the value that should be used for photometry purposes. Then, the magnitude of the source being investigated is an average of the magnitudes determined from each of the four images used to calculate the Stokes parameters ($A, B, C,$ and D).

Chapter 4

The Circumstellar Environments of Herbig Ae/Be Stars

In this chapter, we present the framework around which we will discuss our observations. The observations consist of simultaneous photometric and polarimetric data in the V-band on 11 Herbig Ae/Be stars, with 3 stars chosen for extensive follow-up in B, V, and R. By analyzing the variations in the photometry and polarization that we see in our data, we constrain the geometries of the dusty disks surrounding the stars. Our observations and results are presented in chapter 5. In this chapter, we discuss the difficulties involved in determining the nature of circumstellar disks, and we present some techniques that have been used to gain understanding.

4.1 Herbig Ae/Be Stars

Herbig Ae/Be (HAEBE) stars were first identified by Herbig (1960). They are intermediate mass ($2M_{\odot} - 8M_{\odot}$) pre-main sequence (PMS) stars, and as such, are the intermediate mass analogs to T-Tauris. HAEBE stars have long been recognized as variable, but it has only been in the 2000s that the character and cause of this variation has started to become clear. The uncertainty about the cause of the variations has mainly been a consequence of a lack of understanding of the circumstellar environment

of these stars.

4.1.1 Herbig Ae/Be and T-Tauri stars: Differences and Similarities

To fully understand the difficulty in characterizing photometric HAEBE variations, it is instructive to review the variation mechanisms seen in other PMS stars. T-Tauri photometric variations occur in 3 types. Type 1 variations occur due to the rotation of a star with large cool spots in its photosphere. Type 2 variations occur due to changes in the pattern of accretion hot spots on the surface of the star. Type 3 variations are those that have been coined "UXors" (Herbst et al. 1994), after the canonical example of this type of variation, UX Ori, and are characterized by a set of behaviors that will be listed shortly.[2]

Type 1 and type 2 variations in T-Tauri stars are well understood, and result from a strong, bipolar magnetic field disrupting the accretion disk and diverting infalling matter along flux tubes to accretion zones.

Type 3 variations are only beginning to be understood, and are a result of the circumstellar environment of the stars exhibiting the behavior.

It has been found that while type 1 and type 2 variations seem to be confined to stars classified as T-Tauris, most stars of spectral class G and earlier exhibit some aspects of the type 3 UXor behavior in the form of the following characteristics:

- The timescale for variation increases as compared to that seen in Classical T-Tauri stars.
- There is more variation in V,R,I relative to U and B,
- Light curves go from "irregular" to "quasi-Algol" (Shevchenko et al. 1994).
- The $H\alpha$ equivalent width increases as the star fades in UXors (in type 2 variations these properties correlate).

[2]UX Ori is, in fact a Herbig star, but following the discovery of this phenomenon similar behavior has been seen in a handful of T-Tauris.

- The color index becomes bluer during deep minima in UXors.
- The polarization increases during deep minima in UXors (Grinin et al. 1994).

It has been observed that while type 3 behavior is relatively rare in T-Tauri stars (see, for example Shakhovskoj et al. (2006)), it is observed in $\sim$ 20% of HAEBE stars (Dullemond et al. 2003). This indicates that there may be some fundamental differences between the circumstellar environments of HAEBE stars and those of their lower-mass analogs, although they may also share some characteristics.

4.2 The Dust Obscuration Model of UXor Behavior

In its simplest form, the dust obscuration model surmises that giant dust "clumps" made from protoplanets, protocomets, or another form of circumstellar material periodically occult the central stars, resulting in the observed variations in magnitude, color, and polarization properties (Natta et al. 1997). More recent models describe the variations in terms of a circumstellar disk with a warped geometry (Bertout 2000), a puffed-up inner rim (Isella & Natta 2005) or with a flared or self-shadowed disk (Dullemond et al. 2003). Since the most in-depth studies of disks surrounding young stars have been conducted in the near- and mid- infrared, we now turn our focus to these results.

4.2.1 Near-Infrared Studies of Herbig Ae/Be Stars

Beginning in the early 90's, a debate arose regarding the accretion rate in HAEBE stars, because of an observed IR excess. Some attributed the excess to an accretion disk luminosity (eg. Hillenbrand et al. (1992)), implying a larger accretion rate in these stars. Other groups (eg. Hartmann et al. (1993)) argued that the IR excess was due to thermal emission by circumstellar dust grains not confined to the disk plane. This debate has still not been fully resolved, and remains vitally important

to the investigation of the UXor phenomenon. Fortunately, recent great advances in the understanding of the nature and geometry of circumstellar disks have been made thanks to NIR and mid-IR imaging.

Many PMS objects are surrounded by dusty disks. Dust and gas from the leftovers of star formation concentrates into a protoplanetary disk accreting towards the star. This disk eventually coagulates to form large objects and planets. In this way, the dust traces protoplanetary disks in the IR. In this wavelength regime, direct imaging has proved very useful. The wavelength of the imaging determines the temperature zone and optical depth of the imaged disk. In the inner few AU of the disks, where temperatures can reach $1000K$ or more, dust sublimated or becomes thermally processed, emitting in the NIR. The angular size of this region (on the milliarcsecond scale) has only recently become resolvable.

The first interesting thing to come out of the resolved images was that the size of the NIR region is larger than model predictions (Monnier & Millan-Gabet 2002; Tuthill et al. 2001). This observation implies that there must be an optically thin inner disk hole that is clear of dust because of sublimation (the remaining gas is optically thin). However, there is still more NIR flux from the inner disk than predicted from a flat-disk model, so in addition to needing an inner disk hole, the dust must flare up in the zone where the dust sublimation temperature is reached. This dependencemodel is described by Dullemond et al. (2001). Unfortunately, the NIR observations cannot constrain the geometry of the disk, and there have been alternate interpretations of the observations that challenged the flared-disk geometry. Specifically, it was found by Monnier et al. (2006) that image deviations from symmetrical structure were smaller than predicted by Dullemond et al. (2001). The results of Monnier et al. (2006) favor a model with a curved or puffed-up inner rim as put forth by Isella & Natta (2005) and Dullemond et al. (2003).

Even with this more satisfactory model, the understanding of the disks surrounding HAEBE stars is far from complete. It has been shown (Vinković et al. 2006) that an optically thin halo can explain the NIR-excess without the need for disk puffing, and

the role of any wind component is still unclear. One of the most dramatic results to come out of the NIR studies, however, has been the of the inner disk size on stellar luminosity (Monnier & Millan-Gabet 2002; Monnier et al. 2005). It has been found that when $L_\star < 10^3 L_\odot$, the inner disk radius is where it should be as predicted by models. For the higher-luminosity stars though (when $L_\star > 10^3 L_\odot$), the inner radius is smaller than expected. The explanation for this result given by Monnier et al. (2005) is that higher luminosity objects have optically thick gas present in the inner (dust-free) zone, that shields dust from radiation so that it can survive closer to the star. Many groups have begun to categorize high- and low- L HAEBE stars into two separate categories with different physical processes dominating (Vinković & Jurkić 2007; Monnier et al. 2005; Eisner et al. 2004). In figure 4.1, these two categories are illustrated schematically.

4.3 Problems with Current Models

The preceding discussion has been undertaken to give the reader an understanding of the current models being used to describe the circumstellar environments of HAEBE stars. We now turn to the shortcomings of these models, and specifically, to their inability to adequately explain the UXor phenomenon.

The UXor photometric minima occur due to an increased contribution of light scattered by dust clouds (Natta & Whitney 2000). The temporal properties of the variations indicate that the dust clouds must be located in the inner regions of the disk close to the dust sublimation zone. However, if the inhomogeneities are constrained to the disk, then the disk inclinations must be large (Dullemond et al. 2003). Even the most optimistic inner disk puffing requires inclination angles of $i > 80^\circ$ but imaging data is revealing disks with much smaller angles, as in Shakhovskoj et al. (2005). This study found that the UXor CQTau has an inclination angle of $i = 48^\circ \pm 4^\circ$ in the NIR, $i = 33^\circ \pm 5^\circ$ in the mid-IR, and $i = 60^\circ - 70^\circ$ in the mm. Another UXor, VVSer, was found to have $i = 42^\circ \pm 4^\circ$ in the NIR.

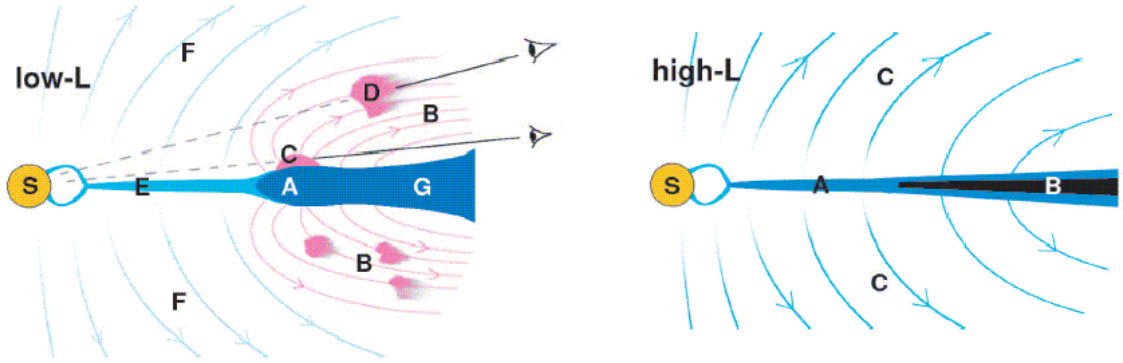

Figure 4.1 Diagram of the two types of inner protoplanetary disk, from Vinković & Jurkić (2007). The image on the left shows the two scenarios that could be responsible for the variations seen in low-luminosity HAEBE stars: (A) a puffed up inner disk rim and (B) a dusty halo outflow. Observations of variability in these stars indicate that either the height of the puffed up rim is variable, causing periodic obscuration of the star (C), or that dust clumps leaving the disk and being blown away by radiation pressure are causing a similar obscuration (D). The disk inside the zone of dust sublimation (E) is optically thin, while the rest (G) is optically thick due to dust. Stellar winds are also present in this scenario (F). On the right is the structure proposed for high-L HAEBE stars. The star is surrounded by an optically thick gaseous accretion disk (A). Dust is confined to the optically thick disk interior (B), while intense stellar and disk winds clear the area of any additional structure (C).

Isella et al. (2006) have argued that disk inclinations are in agreement with the dust obscuration model, using values of $40 - 50°$ for CQTau and $50 - 70°$ for VVSer. However, Vinković & Jurkić (2007) point out that the dust clouds that would be necessary to reproduce the observed effects in those stars would be ≥ 9 and ≥ 4.5 vertical scale heights above the disk, respectively. At these scale heights the dust would decouple from the gaseous disk, and without the effect of gas drag upon it, the dust would be subject to radiation pressure and blown into a halo-like distribution above the disk.

Vinković & Jurkić (2007) propose an alternate model to explain the UXor behavior

- the dusty halo model. In this model, dust clouds are ejected to moderate angles above the circumstellar disk, which explains the weak dependence of photometric variations on i found by Grinin & Kozlova (2000). Additionally, this model accounts for the lack of any dependence between polarimetry observations and i found by Yudin (2000). According to the model of Vinković & Jurkić (2007), dust would rise out of the disk where it would no longer be subjected to gas drag. At this point radiation pressure would take over and blow the dust into a dusty halo-like outflow. Changes in this outflow would manifest themselves as changes in the NIR and mid-IR. The main drawback in the halo model is the lack of any physical mechanism that would allow the dust to overcome the forces of gravity and gas drag and exit the circumstellar disk. This is a serious problem with the dusty halo model, but Vinković & Jurkić (2007) point out that other models have equally serious flaws, such as the inability of the puffed-up rim model of Isella et al. (2006) to reproduce the NIR excess seen in HAEBE stars.

4.4 The Role of Polarimetry Data

Photopolarimetric data is very useful for probing circumstellar disks, since it is sensitive to even a small amount of dust in the line of sight. With many new advances being made through imaging in the NIR and IR, photopolarimetric data is becoming an excellent tool with which to constrain models and to identify interesting objects.

4.4.1 The UXor Effect

The framework explaining the UXor effect arose due to extensive photopolarimetric data, collected mainly at the Crimean Astrophysical Observatory beginning in the mid-1980's and lasting until the mid-1990's (see, for example Grinin (2000) and references therein). The initial observation of what would come to be known as the UXor effect was carried out on the prototype star, UX Ori, by Grinin et al. (1994), and those observations are shown in figure 4.2. The observed increase in polarization accompa-

nied by a decrease in visual magnitude and a blueing in deep minima was initially interpreted as an obscuration by clumps of dust orbiting the stars. Further observations and analysis lead to the models describing the dusty disks around HAEBE stars (Natta & Whitney 2000; Dullemond et al. 2003).

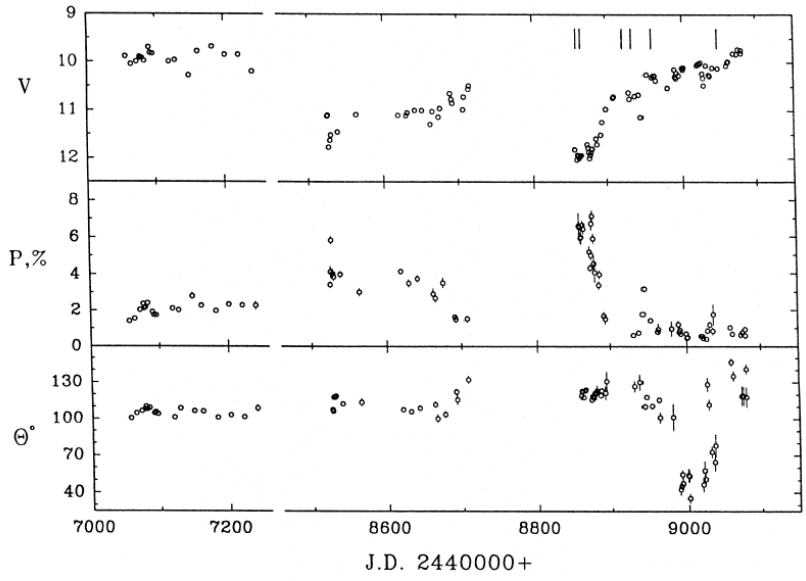

Figure 4.2 Simultaneous photometry and polarimetry observations of UX Ori, from Grinin et al. (1994). The increase in polarization accompanied by a decrease in magnitude and a "blueing" in the overall color (not shown in this figure) are the signatures of the UXor effect, named for this first instance of its observation. The seasons of the observations correspond to 1987-1988, 1991-1992, and 1992-1993.

4.4.2 Dust Grain Properties

The dust found in the circumstellar disks of young stars plays two roles. First of all, the dust on the disk surface determines the fraction of light that is scattered and polarized. Secondly, the dust that obscures the light that reaches the observer directly has a role in determining the wavelength dependence of the light that is directly observed. The dependence on wavelength of P and Δm can constrain disk properties, once the overall geometry is known, and polarimetric data can distinguish

between the sizes of dust grains (Natta & Whitney 2000).

It has been observed (Gledhill et al. 1991) that radiation scattered by large dust grains ($\geq 1\mu m$) has a wavelength-independent polarization fraction, whereas radiation scattered by small grains increased in its polarization fraction as the wavelength increases. Because of this property, polarization observations are able to place limits on the dust grain sizes in disks.

4.4.3 The Geometry of the Emitting Region

The position angle of any observed polarization is an indication of the geometry of the object. Symmetrical objects do not show any polarization due to the cancellation of their polarization vectors, so a non-negative polarization measurement immediately indicates asymmetry. In addition, changes in the position angle of a observed source indicate a change in the geometry of the radiation-emitting region, or a change in the mechanism of polarization (Grinin et al. 1988).

Chapter 5

Observations and Results

We have undertaken an observing program to examine the nature of the circumstellar environment of HAEBE stars through multi-wavelength polarimetry measurements. In this chapter we describe the selection process, the observing campaign, and the results of observations.

5.1 The Selection Process

Program stars were selected from the catalog of de Winter et al. (2001). The following criteria were used to determine inclusion of the stars in the sample set:

1. The stars should be in one of the following categories of PMS stars: T-Tauris, Herbig Ae, or Herbig Be.
2. The stars should be no fainter than ~ 15 mag.
3. The stars should have shown some previous photometric variability.
4. In order to take advantage of the PROMPT polarimeter's coverage of the southern hemisphere, stars with southern declinations should be given preference.
5. The sample should include some stars that have been observed polarimetrically in the past, as well as those with no prior polarimetric observations.
6. The right ascension of the stars should be such that they will be observable during the months of the observing program (March-June 2007).

After considering the criteria, the following 11 stars were selected for observation: 7 Herbig Ae stars (UX Ori, NX Pup, HD132947, V865 Sco, KK Oph, HD163296, WW Vul), and 4 Herbig Be stars (HD98922, HD76534, KR Mus, SS73 44).

Star ID	Alt. ID	α (2000)	δ (2000)	#Obs.	Av. P(%)	Δ P(%)
UX Ori	HD 293782	05 04 30.0	-03 47 14	7	3.1	1.4-4.2
NX Pup	CD-44 3318	07 19 28.3	-44 35 11	14	1.7	1.0-3.1
OU Vel	HD 76534	08 55 08.7	-43 28 00	7	0.5	0.5
HD 98922	Hen 3-644	11 22 31.7	-53 22 11	8	0.4	0.2-0.6
KR Mus	HD 100546	11 33 25.4	-70 11 41	7	0.3	0.3-0.4
SS73 44	vdBH 65b	15 03 23.9	-63 22 54	14	4.7	3.7-5.8
HD 132947		15 04 56.1	-63 07 53	4	1.1	1.0-1.1
V865 Sco	HD144668	16 08 34.3	-39 06 18	5	0.9	0.9
KK Oph	Hen 3-1346	17 10 08.1	-27 15 18	14	3.6	2.2-4.7
HD 163296	MWC 275	17 56 21.3	-21 57 22	4	0.1	0.1
WW Vul	HD 344361	19 25 58.8	+21 12 31	20[1]	1.0	0.9-1.2

Table 5.1 Stars in the Observing Program. The first two columns are the star identifiers, columns 3 and 4 are the RA and DEC, column 5 is the number of times the star was observed in the V-Band, and columns 6 and 7 are the average polarization and the range of polarization observed. (1) WW Vul was the only star that was observed multiple times per night.

5.2 The Observing Campaign

During the months of March and April 2007, an initial set of observations was carried out, with each star being imaged between 4-10 times. All initial observations were carried out in the V-Band. One star, WW Vul, was imaged multiple times each night to search for short-term variations, while all other stars in the program were imaged no more than once per night. Following analysis of the initial results, 3 stars

were selected as objects of interest (NX Pup, SS73 44, and KK Oph), and during the months of May and October 2007 these 3 stars were imaged repeatedly in V, B and R.

5.3 Three Sources of Interest

In the following sections we present the results of the observing campaign carried out on our three sources of interest: the Herbig Ae stars NX Puppis and KK Opiuchus, and the Herbig Be star SS73 44. Some of the characteristics of these three stars are listed in table 5.2 We have given each of these stars its own section, in order to discuss the unique properties of each one, but before we enter into the details of the individual stars, we will outline some of the global characteristics that we searched for in the data.

Throughout our observations we looked for several different signatures that would reveal the nature of the circumstellar environments of the chosen stars. First of all, we were looking for an increased level of polarization accompanied by a decrease in magnitude and an increased reddening of the star. This signature is interpreted in the puffed-up inner rim models of Dullemond et al. (2003); Isella & Natta (2005) as an obscuration by dust of the central source, resulting in an increase in the relative contribution to the total flux by scattered light from a circumstellar disk. Since the scattered light is polarized, the increased relative contribution to the total flux by this component reveals itself by an increase in the % polarization. The overall reddening and decrease in magnitude are a result of the dust obscuration. This observation can also be explained by the dusty halo outflow models of Vinković & Jurkić (2007), as the result is the same regardless of the source of the obscuring dust.

The next signature that we were looking for throughout our observations was a "blueing" effect at extreme photometric minima, accompanied by a dramatic increase in the polarization. In the Dullemond et al. (2003); Isella & Natta (2005) models, this observation is a consequence of heavy dust obscuration of the central source to such an extent that scattered light from the surrounding disk dominates the total

Table 5.2 Properties of the 3 stars chosen for follow-up observations in B, V and R.

Star ID	D (kpc)	L ($L_\odot$)	Age (Myr)	M ($M_\odot$)	Spectral Type	Binary y/n?	Binary Sep.	Assoc. SFR	i Disk	P_{ism} (%)	θ_{ism} (°)	Refs.[e]
NX Pup	0.45	16-19	3-5	2	F0-F2	y	60 AU	Gum Neb.	0°[a]	0.28	38	1,9
KK Oph	0.16	35	7	1.6	A6Ve	y	258 AU	Barnard 59	70°[b]	0.13	179	2,3,4,5,9
SS73 44	2.9[c]	(2.4×10^3)[d]	-	-	Be pec.	n	-	Circinus	-	-	-	6,7,8

[a]Inclination of the binary system is assumed at 0° based on direct observation.

[b]Best estimate made by Leinert et al. (2004), based on fitting the models of Dullemond et al. (2001) to mid-IR data.

[c]The distance to the Circinus Molecular cloud is uncertain by a factor of nearly 1.5

[d]Based on an assumed distance of 2.9 kpc.

[e]References are as follows: (1) Schoeller et al. (1996) and references therein, (2) Leinert et al. (1997), (3) Carmona et al. (2007), (4) Leinert et al. (2004), (5) Herbig (2005), (6) Ray & Eisloeffel (1994), (7) Gahm & Malmort (1980), (8) Manchado et al. (1990), (9) Maheswar et al. (2002).

flux. This type of observation does not completely rule out the dusty halo outflow model (Vinković & Jurkić 2007), although that model has more trouble explaining a mechanism that would produce dust outflows that are both clumpy and dense enough to reproduce such an observation.

Another signature of importance has to do with the position angle (PA) of the polarization. The PA is a measure of the geometry of the system under investigation, and a changing PA is an indication of a change in the geometry of the system. A smooth change in PA accompanied by a change in magnitude and/or polarization can indicate the presence of two polarized components (with different PAs) that contribute to the polarization in a way that varies as a function of time (Bastien 1981). Abrupt changes in the position angle that are not accompanied by a change in any other parameters can indicate that the radiation is being produced in a different region close to the star. Another important role that the PA can play is to reveal the orientation of dusty structures in the plane of the sky. If the disk is optically thin, and the polarization is produced by single scattering, then the position angle of the linearly polarized light will be perpendicular to the disk. On the other hand, if the disk is optically thick, the polarization will be produced in the light scattered by dust distributed perpendicularly to the disk, resulting in a polarization PA that is parallel to the disk (Bastien 1987; Maheswar et al. 2002). Polarization vectors perpendicular to the disk plane can also be produced by scattering off the surface of an optically thick disk.

The fourth property that we monitored over the course of our observations was the dependence of the level of polarization on wavelength. We did polarimetry in the B, V and R bands in order to observe this dependance. Interstellar polarization follows a clear wavelength dependance that changes according to the properties of interstellar dust grains – this is known as Serkowski's Law (Serkowski 1973). In sources that have some level of intrinsic polarization, the wavelength dependance of the polarization deviates from that law. Both the intrinsic linear polarization and the PA can be a function of wavelength, and their relationships can be used to determine

dust parameters (Bastien 1981; Natta & Whitney 2000).

The final signature that we looked for in our observations was a periodicity in the temporal evolution of any of the parameters that we measured (% polarization, PA, magnitude, color). These parameters could change in a perodic way if the variations were being produced by hot or cool spots on the surface of the rotating star, if there was a precessing of the circumstellar disk, or if the star's environment was subject to periodic flaring or infalling episodes. In the puffed-up inner rim model of Dullemond et al. (2003); Isella & Natta (2005), variations are caused by turbulence in the hot inner rim of an accretion disk, and no periodicity is expected to be observed. Likewise, the dusty halo outflow model of Vinković & Jurkić (2007) produces variations in a random way as the outflows obscure the stellar radiation, and once again no periodicity is expected.

Now that we have outlined some of the features that we sought to observe in our data, we will turn to a detailed discussion of each of the three stars that were chosen as interesting targets for follow-up observations, and to the data that we collected from them.

5.4 KK Oph

Located in the constellation Ophiuchus (the serpent holder), KK Oph is spectral type A6Ve Herbig Ae star that has been well-studied due to its large photometric variations ($\Delta V > 3$mag). KK Oph was one of the stars studied by the ROTOR program carried out at Mount Maidanak Observatory in Uzbekistan (Herbst & Shevchenko 1999). Between the years 1983 and 1998 this star was observed 530 times in U, B, V, and R filters. KK Oph was found to be one of the most photometrically active HAEBE stars in the ROTOR program's sample of 230, and it displays one of the most unusual light curves (figure 5.1). Although there are variations in the star's magnitude every season, KK Oph experienced an extended brightness peak in the early 1990s. It had been fainter prior to that time, and has since faded once again. The color-magnitude

diagram for KK Oph is also interesting, showing a strong color turnaround effect in all colors, with a distinct "blueing" at its faintest (figure 5.2).

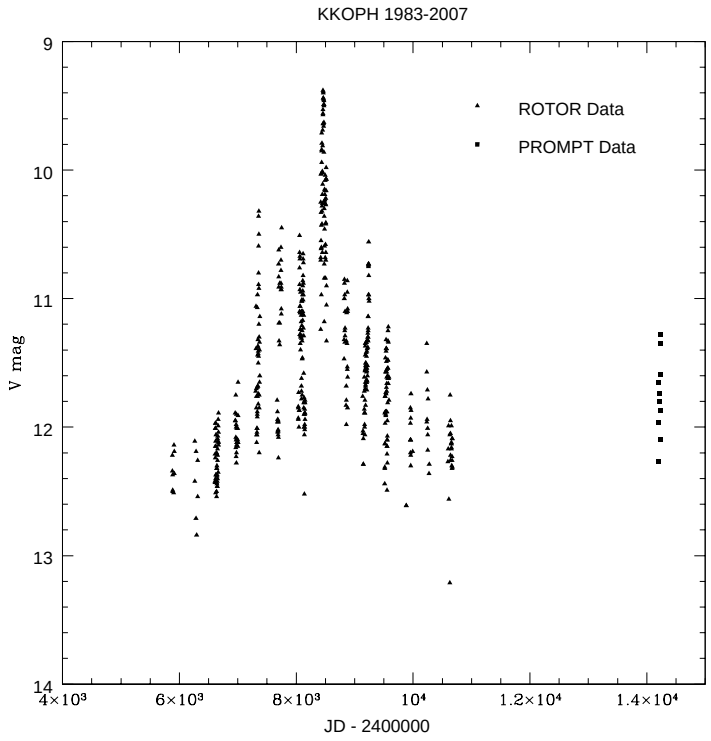

Figure 5.1 The light curve of KK Oph from 1983-2007, with data from the ROTOR program (Herbst & Shevchenko 1999), and our PROMPT data.

Despite the extensive photometric data on this star, very few polarimetric observations have ever been carried out on it. Prior to the PROMPT observations, the polarimetric data consisted of 3 data points in 1994 (Yudin & Evans 1998), and 9 data points in 1998 (the EXPORT project; Oudmaijer et al. (2001)). While the 1994 data shows little polarimetric variability (figure 5.3), the 1998 data shows some evidence of UXOR behaviour (an increase in polarization accompanied by a decrease in magnitude and a reddening). However, the faintest photometric data point in the EXPORT study is also the one with the lowest polarization value - a result that is contrary to the expectations of the UXOR model. This behaviour is shown in figure 5.4. Additionally, the EXPORT study detected a change in the position angle of

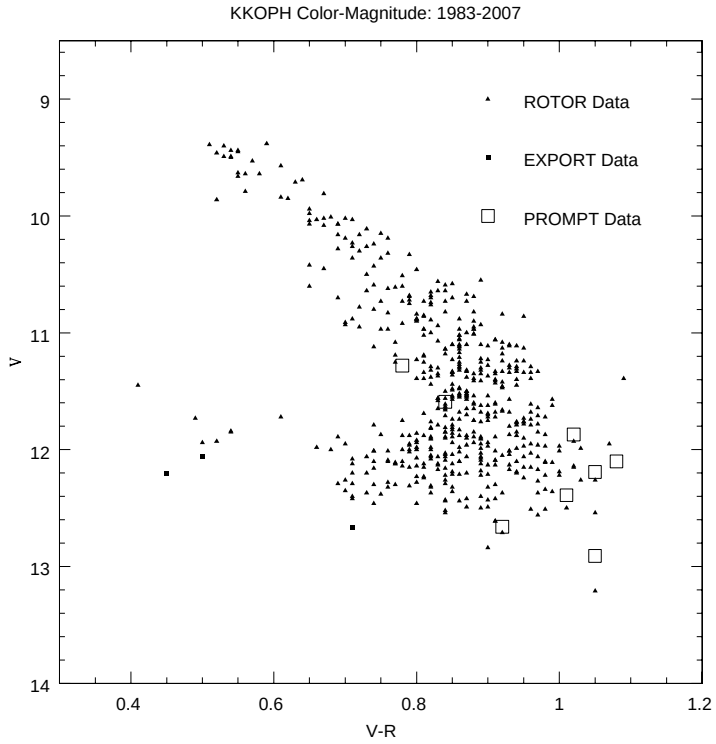

Figure 5.2 The color curve of KK Oph from 1983-2007, with data from the ROTOR program (Herbst & Shevchenko 1999), the EXPORT program (Oudmaijer et al. 2001), and PROMPT data.

the polarization vector between their two observation runs, perhaps indicating that the source of the polarization changed during this time period.

Our data on KK Oph, presented in figure 5.5 continues to display slightly contradictory results. On the one hand, the faintest data point is the one with the highest level of polarization, and the brighter points tend to display lower levels of polarization. We also detect a trend of increased reddening with decreasing brightness. Both of these results are consistent with obscuration events. On the other hand, our data demonstrates that there is not always an anti-correlation between magnitude and polarization levels, as would be expected if obscuration events were the sole source of the polarization. We did not detect the change in position angle that was observed by the EXPORT study, nor did we detect the "blueing" effect seen by Herbst & Shevchenko

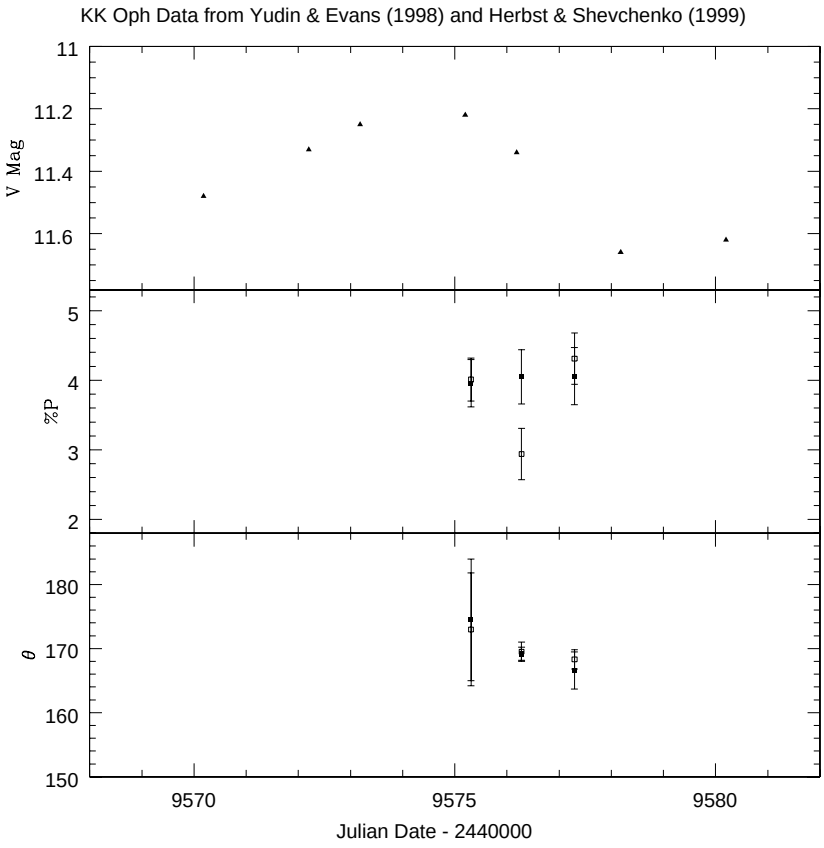

Figure 5.3 The polarimetric behaviour of KK Oph as observed by Yudin & Evans (Yudin & Evans 1998). Filled squares are observations in the V-Band, while open squares are R-Band. The photometric data in the top panel is from Herbst & Shevchenko (1999).

(1999).

5.4.1 Using the Position Angle of the Polarization to determine Disk Orientation

As was described earlier in this chapter, the PA of the linear polarization vector is often aligned either perpendicular or parallel to the orientation of the disk in the sky. In the case of KK Oph, this information can be interperted in the context of the position angle of its binary companion, which was first identified by Pirzkal et al.

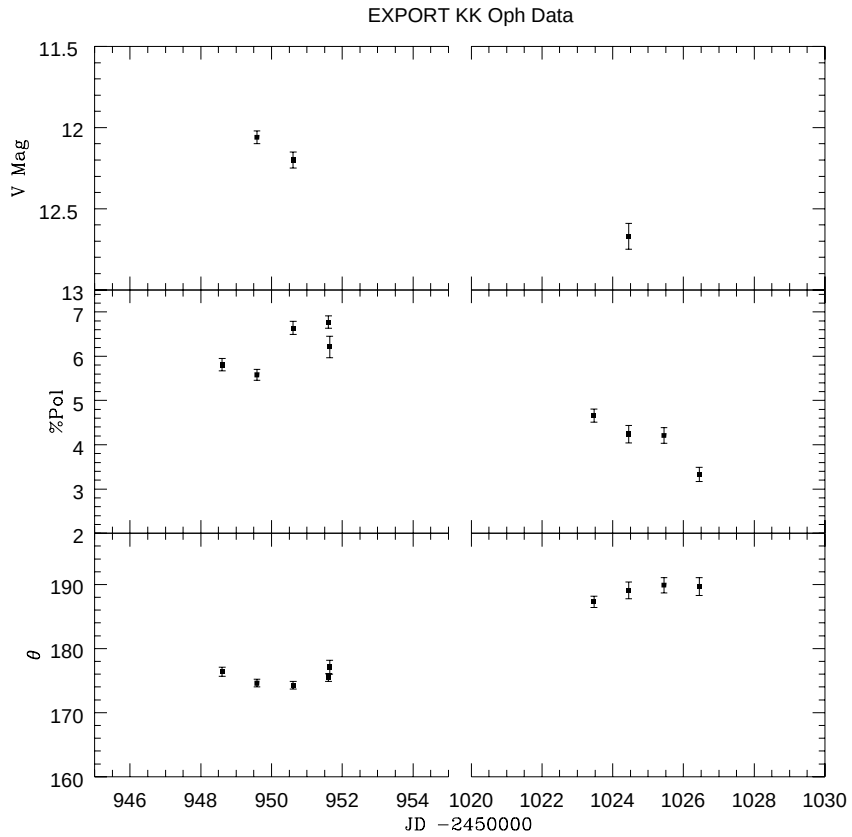

Figure 5.4 The polarimetric and photometric behaviour of KK Oph as observed by the EXPORT program in 1998 (Oudmaijer et al. 2001). The first set of observations corresponds to May 1998 and the second set is from July 1998.

(1997), and independently by Leinert et al. (1997). KK Oph's binary companion is a classical T-Tauri star, separated from the primary by 1.61″ (258 AU at a distance of 160 pc). The position angle of the line connecting the primary and the secondary is given as 257° by Pirzkal et al. (1997), and 247.2° by Leinert et al. (1997).

Inspection of figure 5.5 reveals that the PA of our polarimetry observations stayed relatively constant, at an average angle of 170°. This value falls within 3° of being perpendicular to the plane of the binary system as calculated by Pirzkal et al. (1997), and within 13° of the plane as calculated by Leinert et al. (1997). Our observations therefore indicate that we are observing polarization either by single scattering through

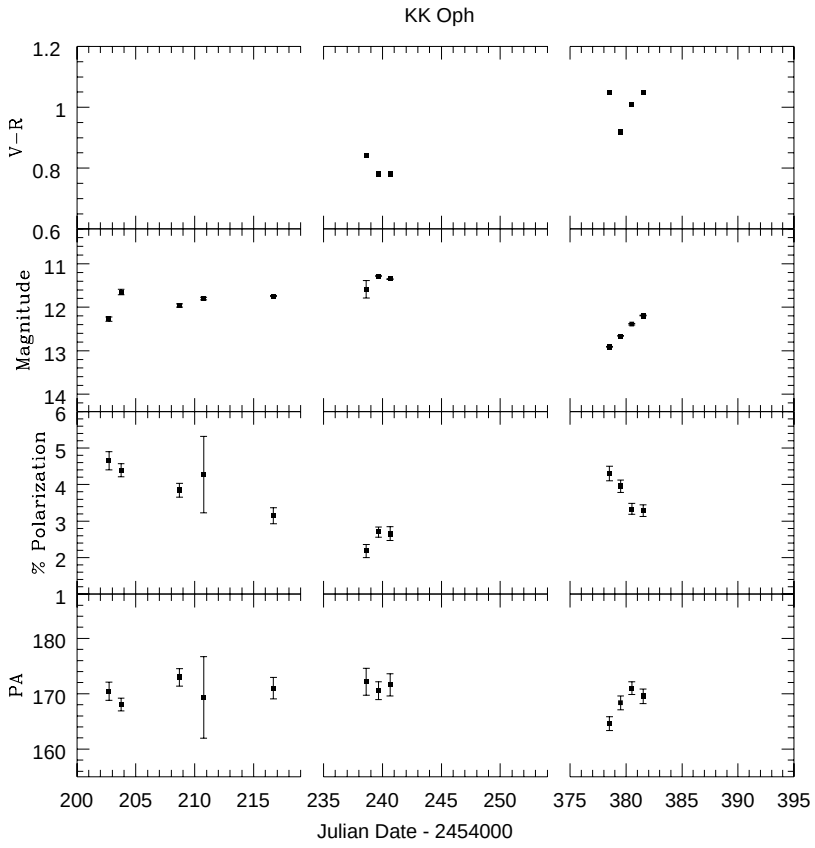

Figure 5.5 Simultaneous polarimetry and photometry data from KK Oph, taken with the PROMPT polarimeter from April-October 2007. The first observing season corresponds to April 2007, the second is May 2007, and the last is October 2007. All data presented here is V-Band.

an optically thin disk, or by scattering off the surface of an optically thick disk. In either case, the disk is coplanar with the orbital plane of the binary system.

We note that this calculation of the relationship between the orbital plane of the binary sytem and the orientation of the circumstellar disk was carried out by Maheswar et al. (2002) for KK Oph based on the results of the EXPORT data (Oudmaijer et al. 2001). However, the EXPORT data contains a shift in PA between their two observing seasons, and they had insufficient data to determine if either of the two angles were preferred by the system. Our data indicates that the majority of the polarization is

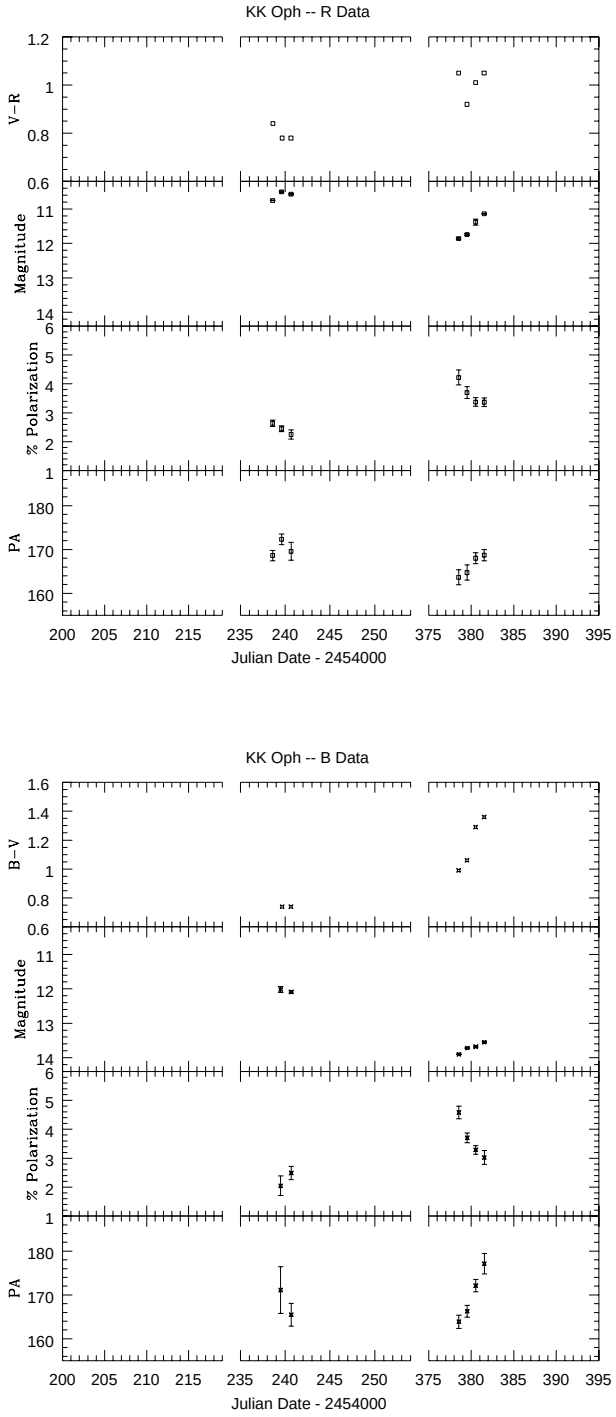

Figure 5.6 Simultaneous polarimetry and photometry in the R (top) and B (bottom wavebands, from the PROMPT polarimeter.

generated at a PA of 170°, and suggest that the PA change observed by Oudmaijer et al. (2001) was the result of the introduction of a new, transient polarization source to the system.

5.5 NX Pup

In the constellation Puppis (the stern of the great ship Argo), lies the second star chosen for our follow-up campaign: NX Pup. NX Pup is actually a close HAEBE binary with the two components of the system separated by only 126 milli-arcseconds ($\approx$ 60AU). The primary, NX Pup A, has been identified as a spectral type F0-F2. It has a mass of $2M_{\odot}$ and an age of 3-5 Myr (Schoeller et al. 1996). NX Pup is located at the head of the cometary globule CG1 (figure 5.7), in the much larger Gum nebula. Analysis of the chemical and kinematic properties of CG1 indicate that both NX Pup A and B formed considerably before the nebula reached its current morphology (Schoeller et al. 1996).

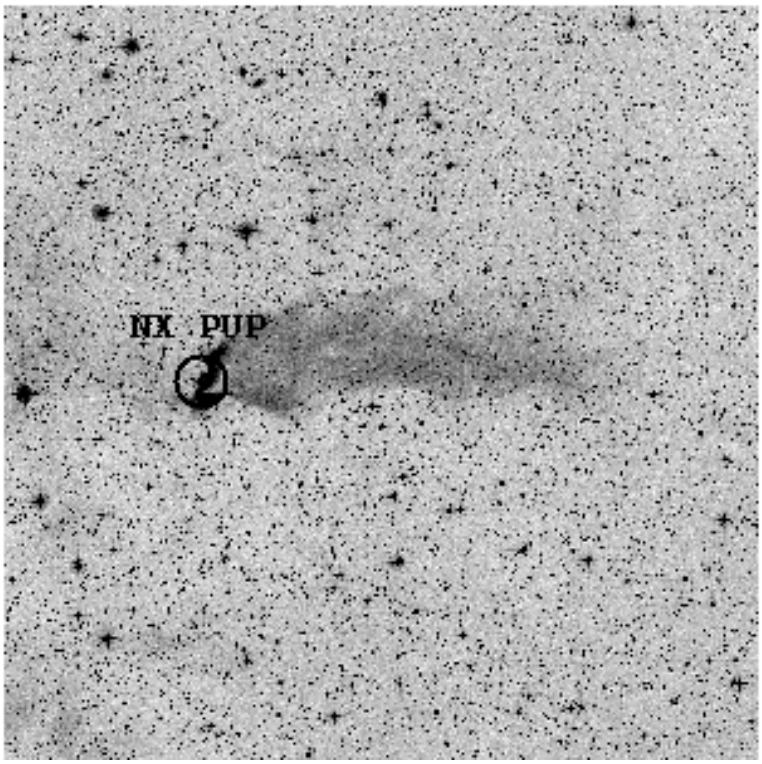

Figure 5.7 NX Pup shown at the head of the cometary nebula CG1. The field of view of this image is $(0.75^{\circ})^2$. The center of the Gum nebula lies 10° to the east of this image.

NX Pup was studied in the ESO's Long-term photometry of variables project

(LTPV) (Manfroid et al. 1991, 1995; Sterken et al. 1993, 1995). From October 1982 until March 1993 the star was observed in the Strömgren *ybvu* system a total of 355 times. The light curve and CM diagram from these observations can be seen in figure 5.8 and figure 5.9.

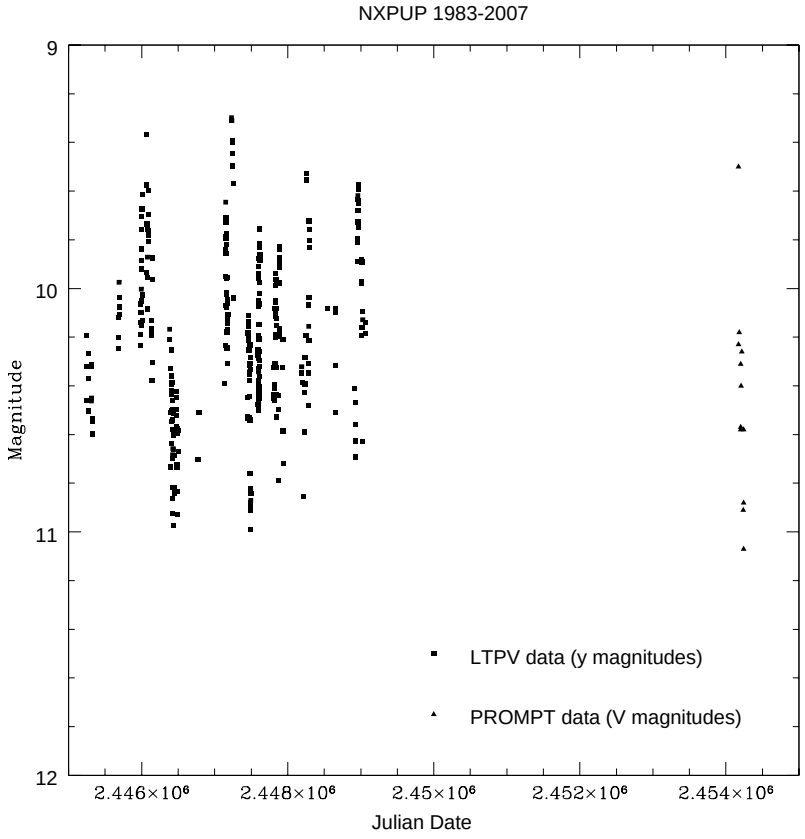

Figure 5.8 The light curve of NX Pup, including data from the LTPV project as well as PROMPT data. The LTPV data is taken in the Strömgren y filter; PROMPT data is taken in Bessel V.

As noted in the LTPV analysis, NX Pup shows a large photometric variability ($\Delta y = 1.7$mag), yet no dependence of color index on visual brightness (Bibo & The 1991). Bibo and Thé note that NX Pup is the only star in their list of 23 HAEBE candidates with magnitude variations larger than $\approx$ 2mag with no correlation between color and brightness.

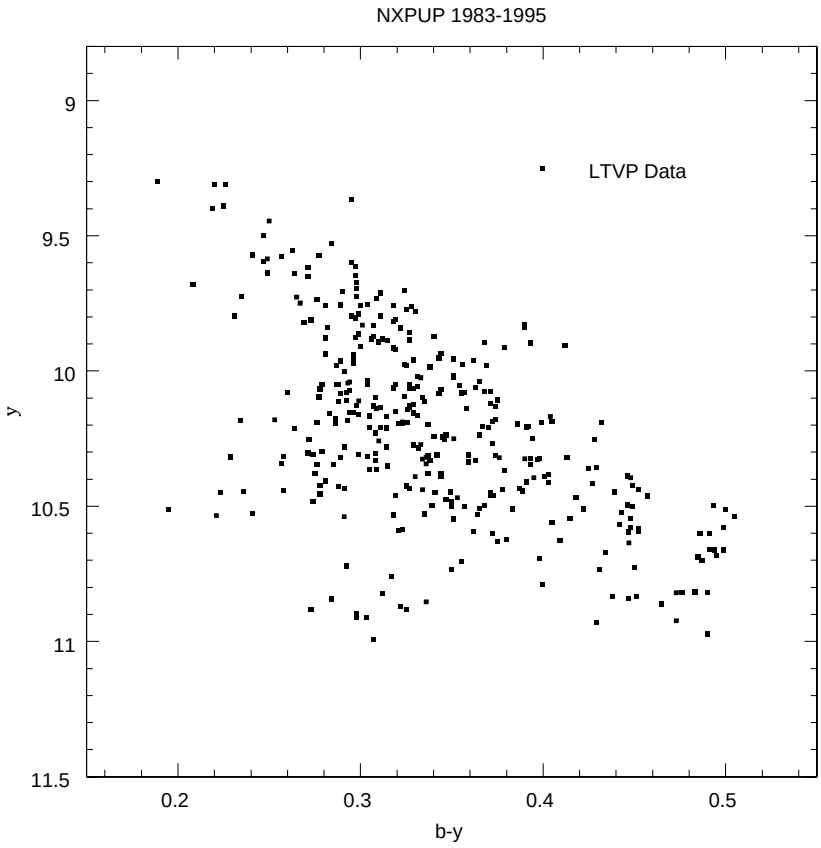

Figure 5.9 The CMD of NX Pup, from LTPV data. There is no apparent color-magnitude relation.

Prior to our study, only 2 polarimetric observations had been made of this star, in January 1995 (Yudin & Evans 1998). Their observations are shown in figure 5.10, and show only a low level of polarization (% P $\approx$ 0.7) with no significant change in polarization. Our study therefore represents the most complete polarimetric data set of this star to date, and the first instance of observed polarimetric variability.

The V band NX Pup data from the current study is presented in figure 5.11. Data from the B and R bands is shown in figure 5.12.

The PROMPT data shows a general trend of an increase in polarization with a decrease in magnitude in all three wavebands, which is interpreted as the result of a dust obscuration event. Unlike KK Oph, however, changes in the degree of polarization

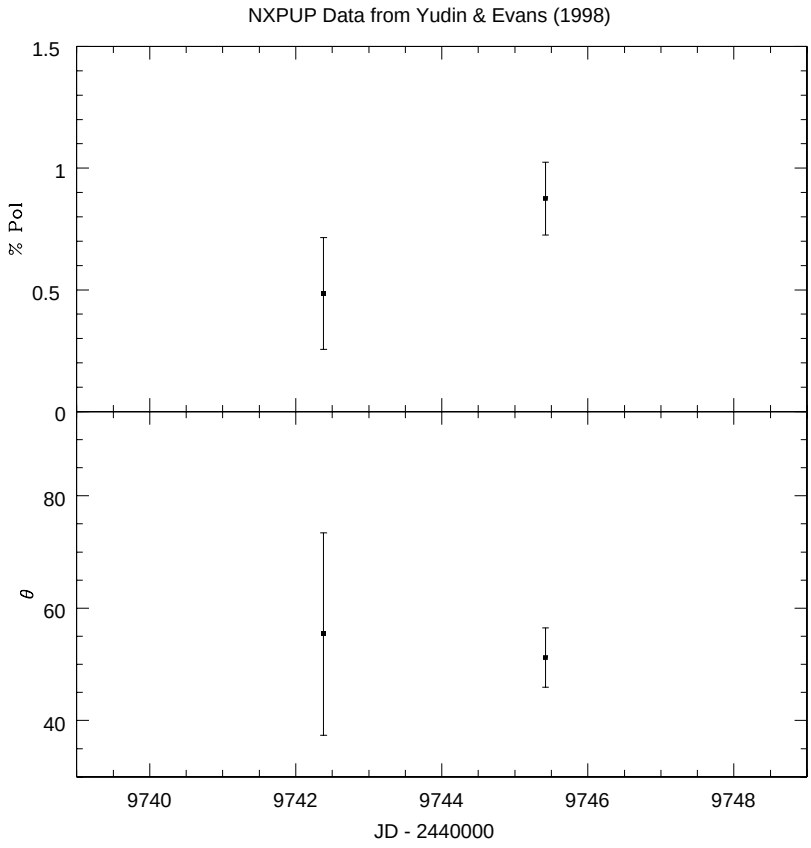

Figure 5.10 The only measurement of polarization in NX Pup prior to the current study, from Yudin & Evans (1998).

of NX Pup are almost always accompanied by a change in the position angle - an indication of a changing geometry in the structure that produces the polarization. There are likely two polarization sources present in the vicinity of NX Pup (each with its own position angle), and as the relative contribution of those two sources to the overall flux changes, so do the polarization and the position angle.

5.5.1 Investigating the source of the polarization

Like KK Oph, NX Pup has a binary companion. The companion is a type F7-G4, $1.75 M_{\odot}$ object, located 60AU from the primary (based on a distance of 450 pc), at a position angle of 62° (Schoeller et al. 1996). Observations of NX Pup and its binary

companion have assumed that the system is seen "face-on", ie. at an inclination angle of 0°, but the lack of any detectable orbital motion over a time-period of three years (1993-1996), have caused this assumption to be re-evaluated (Schoeller et al. 1996). The inclination of orbital plane of the system can therefore be considered to be an unknown quantity.

As can be seen in figure 5.11, the position angle of the polarization varies between 30° and 60°. It does not appear that there is a component of the polarization with its polarization vector perpendicular to the line connecting the primary and secondary in the plane of the sky. However, the upper and lower bounds of the position angle are not without significance. The upper bound of the PA fluctuations corresponds roughly (to within $\approx 5°$) to the PA of the separation of the binary components. On the other hand, the lower bound of the PA fluctuations corresponds roughly (again to within $\approx 5°$) to the PA of the interstellar polarization, calculated by Maheswar et al. (2002) to be $P_{ism} = 0.28\%$ and $\theta_{ism} = 38°$. More observations are required to verify if these associations (particularly the upper bound) are real, but the data obtained thus far is very interesting. A component of polarization that is parallel to the interstellar polarization implies that the circumstellar region of NX Pup has been influenced by the large-scale $\vec{B}$ fields in the area.

An additional interesting aspect of the polarization of NXPup is the dependance of the degree of polarization on the PA (figure 5.13). The highest levels of polarization occur at the minimum PA, while lower levels of polarization are observed with increasing PA. The most likely cause of this correlation is the presence of two competing sources of polarization in the system. This observation gives additional interest to the possible significance of the lower and upper bounds of the PA discussed in the previous paragraph.

A final aspect to consider when analyzing NX Pup is the possibility that the secondary has influenced the shape of the disk surrounding the primary, resulting in an asymmetry in the dust distribution, or in a warping of the disk. An asymmetrical disk, even when viewed face-on, whould show some level of polarization because of the

non-cancellation of the polarization vectors.

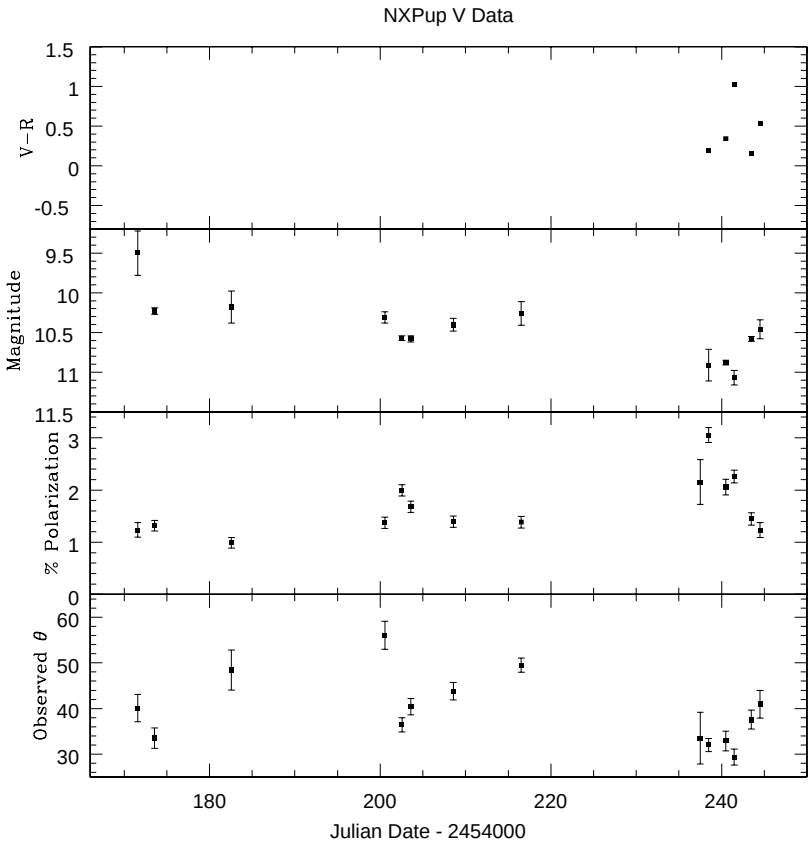

Figure 5.11 Simultaneous photometry and polarimetry data of NX Pup, obtained with the PROMPT polarimeter. All data shown here is taken in the V waveband. Changes in polarization are almost always accompanied by a change in position angle in all three wavebands, indicating a changing geometry in the polarization-producing structure.

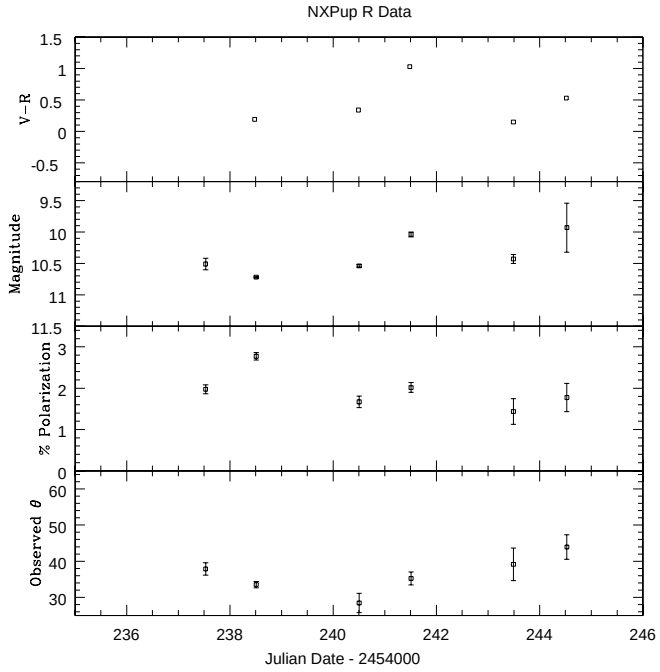

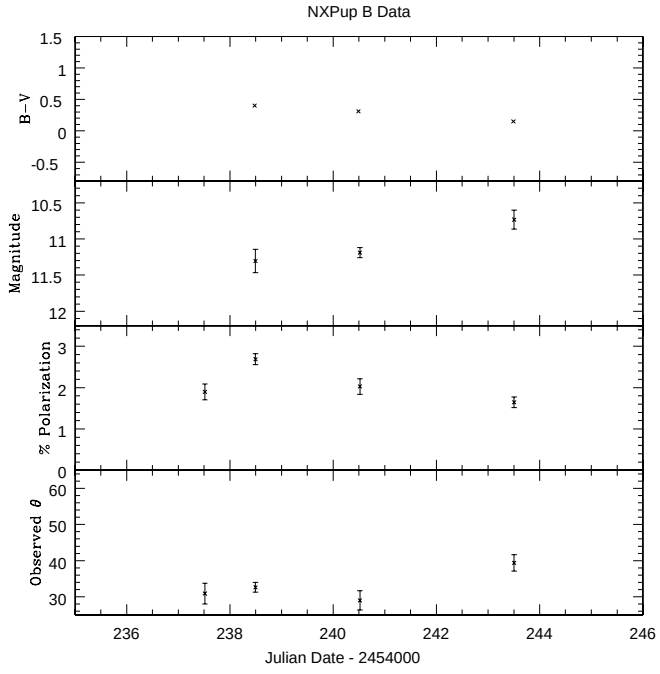

Figure 5.12 Same as figure 5.11 except with the data from the R (top) and B (bottom) wavebands plotted separately for the nights in which multiple waveband observations exist.

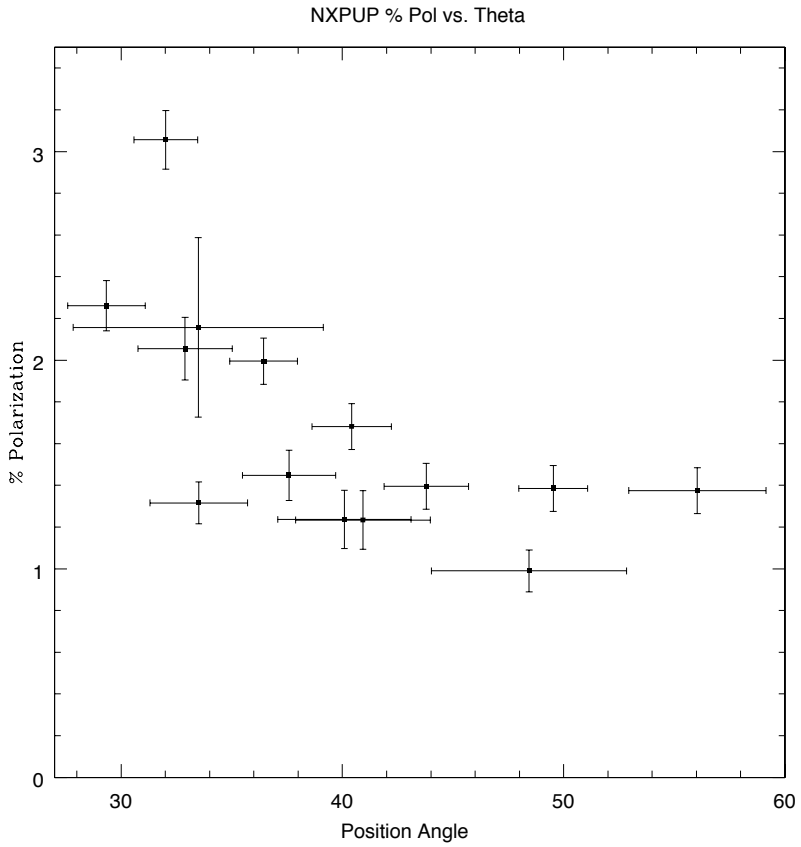

Figure 5.13 The dependance of position angle on polarization for NXPup.

5.6 SS7344

SS73 44 is the 44th star to be classified in the 1973 list by Sanduleak and Stephenson (Sanduleak & Stephenson 1973). It is also known as vdBH 65b, IRAS 14592-6311, and HBC 596. In the 1973 classification, it was originally thought to be a symbiotic star. However, subsequent studies by Allen (1978) and Gahm & Malmort (1980) demonstrated that it has the spectrum of a PMS star, in addition to an IR excess consistent with emission from circumstellar dust, and mass-loss inferred from P-Cygni profiles in the H, HeI, FeII and CaII lines. Additional discoveries of the association of SS73 44 with a cometary nebula and the presence of a weak variable H_2O maser (Scalise et al. 1981) confirmed its identity as a PMS object, and based on its inferred luminosity, it was classified as a HAEBE star (Manchado et al. 1990). SS73 44 was classified in the catalogues of The et al. (1994) and de Winter et al. (2001), as a HAEBE star, with a photometric range of $\Delta V = 14.75 - 16.80$. A spectroscopic study of SS73 44 by Pereira et al. (2003) revealed a reddened continuum with many lines in emission, and the Balmer lines in the blue end of the spectrum showing P-Cygni profiles.

SS7344 was initially chosen for follow-up observations after initial results indicated a high ($P \approx 4\%$) level of polarization.

5.6.1 The Association of SS73 44 with Herbig-Haro object 140

SS73 44 is located in the Circinus cloud, an active star-forming region described by Sandqvist (1977) and shown in figure 5.14. Ray & Eisloeffel (1994) discovered 4 Herbig-Haro (HH) outflows in the Circinus cloud associated with SS73 44, which they labeled as HH140A-D. An HH outflow is an ejection of gas from a young star, arising as a consequence of gas from an accretion disk reaching a hot, rapidly rotating inner disk region. At this point, the gas is ejected in highly collimated polar jets that collide with the surrounding ISM, producing shock waves that are detectable by millimeter-

wave observations. HH objects are commonly found in association with T-Tauri stars, but their association with the higher mass HAEBE stars is less common. In addition to being associated with a type of star that does not normally produce these types of outflows, the HH objects associated with SS73 44 are unusual due to the fact that they are contained within a cone-like reflection nebula associated with the star, but they are not highly collimated, as is generally observed in HH outflow regions (Ray & Eisloeffel 1994). However, there appears to be a common outflow direction within that region of the cloud, with PA=135°. The outflows were further investigated by Bally et al. (1999), who derived the mass, velocity, and total energy contained in the outflows.

The presence of these outflows imply the presence of a disk surrounding SS73 44. Furthermore, since HH outflows are polar jets that are ejected perpendicularly to the disk, if either the jet inclination or the disk inclination are known, the other can be inferred. The inclination of the jets has been listed as $\sim 60°$ by Bally et al. (1999), but that inclination angle was only picked because it is statistically the most probable angle at which to observe a jet.

5.6.2 The Photopolarimetric Behavior of SS73 44

We have observed a slow trend of a decrease in brightness from $V = 12.7$ to $V = 13.0$, with an accompanying increase in polarization from 3.8% to 6.0% over a time period of $\approx$ 180 days. Additionally, there was an isolated event of a sudden increase and subsequent decrease in polarization in the B waveband on JD 2454238.5. Our data set represents the most extensive set of photometric observations of this star to date, and the first polarization measurements. Our results in the V waveband are shown in figure 5.15, while B and R results are presented in figure 5.16.

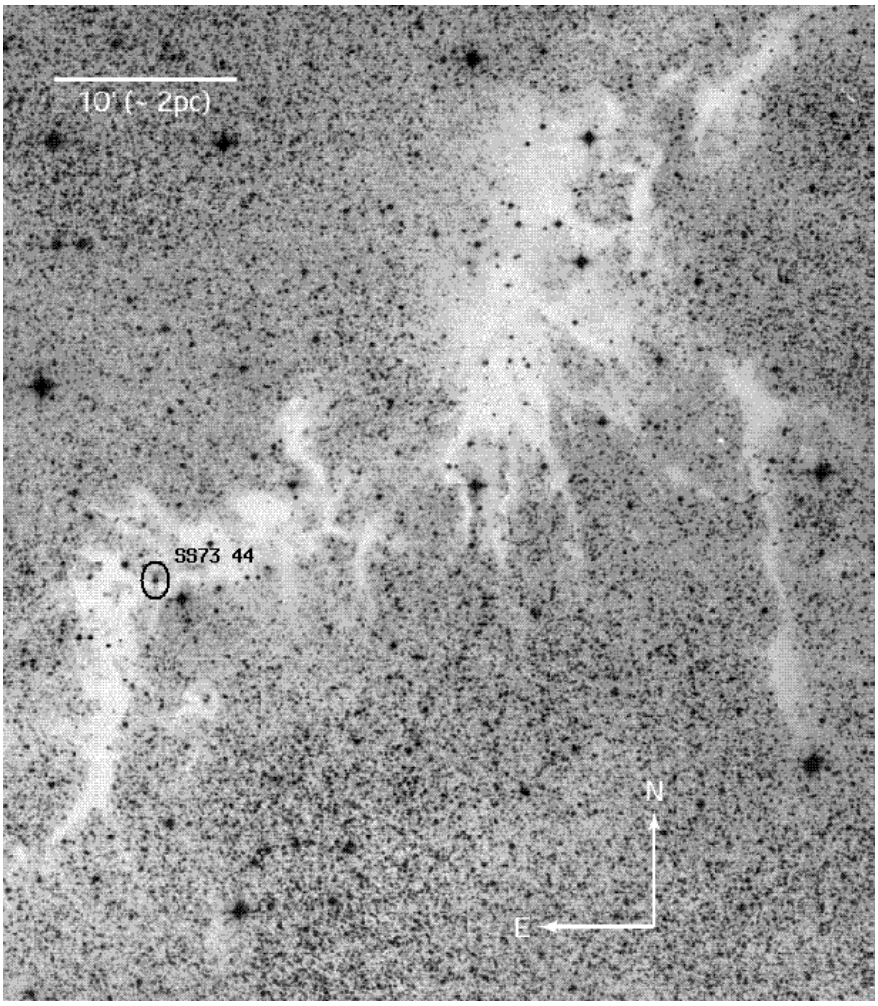

Figure 5.14 An R-Band ESO Schmidt photograph of the western portion of the Circinus cloud (Bally et al. 1999), with the position of SS74 33 marked.

5.6.3 Intrinsic polarization in SS7344

A first glance at the SS7344 data led us to believe that the observed high level of polarization was due solely to interstellar polarization, and not due to any intrinsic polarization of the star. To verify that initial feeling, we modeled the change in polarization as a function of wavelength. Interstellar polarization is known to follow the relation known as Serkowski's Law (Serkowski 1973):

$$p_\lambda = p_{max} \exp[-K \ln^2(\lambda_{max}/\lambda)] \tag{5.1}$$

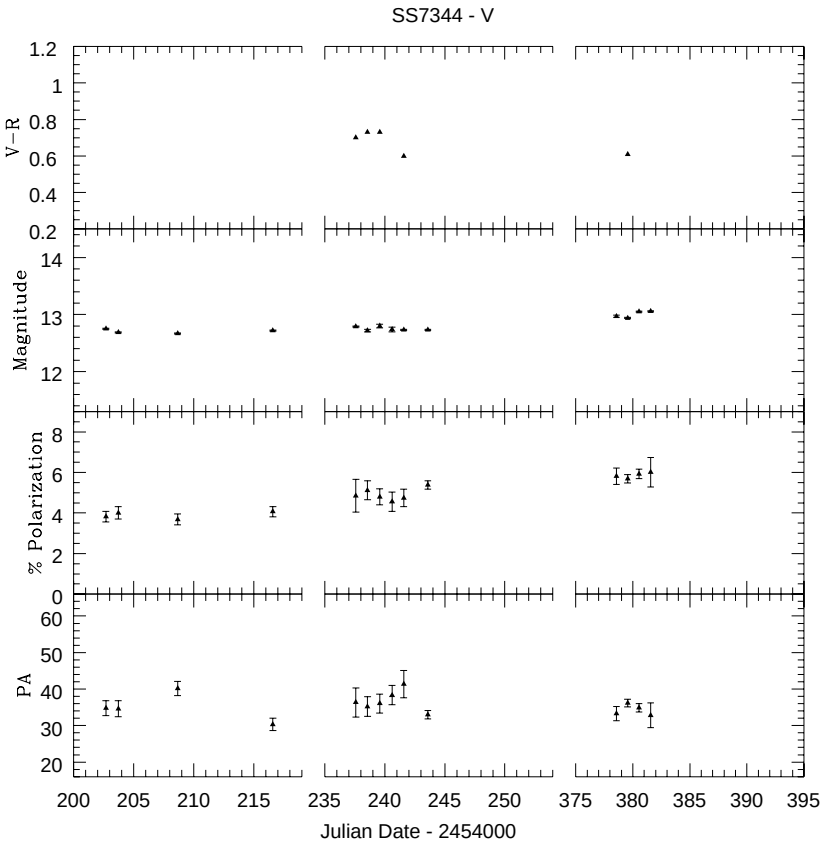

Figure 5.15 PROMPT V-band polarimetry data from SS7344. The data shows a slow upward trend in polarization, accompanied by a decrease in brightness of 0.3 mag. The position angle is unchanged.

The results of fitting our data to Serkowski's law are shown in figure 5.17. It can be seen that our data does not fit well with the expected results if the polarization of this star is due entirely to interstellar polirization. Due to the very slow and relatively small changes in the total polarization and the photometric magnitude of this star, and no changes in the position angle, the best explanation for the observations is that this star is surrounded by a nearly face-on dusty disk, a case in which very few dust obscuration events would be expected to occur. Alternately, SS7344 may be surrounded by a disk of the type described by Vinković & Jurkić (2007), in which no puffed-up rim can exist due to the presence of intense stellar winds and radiation pressure. In this

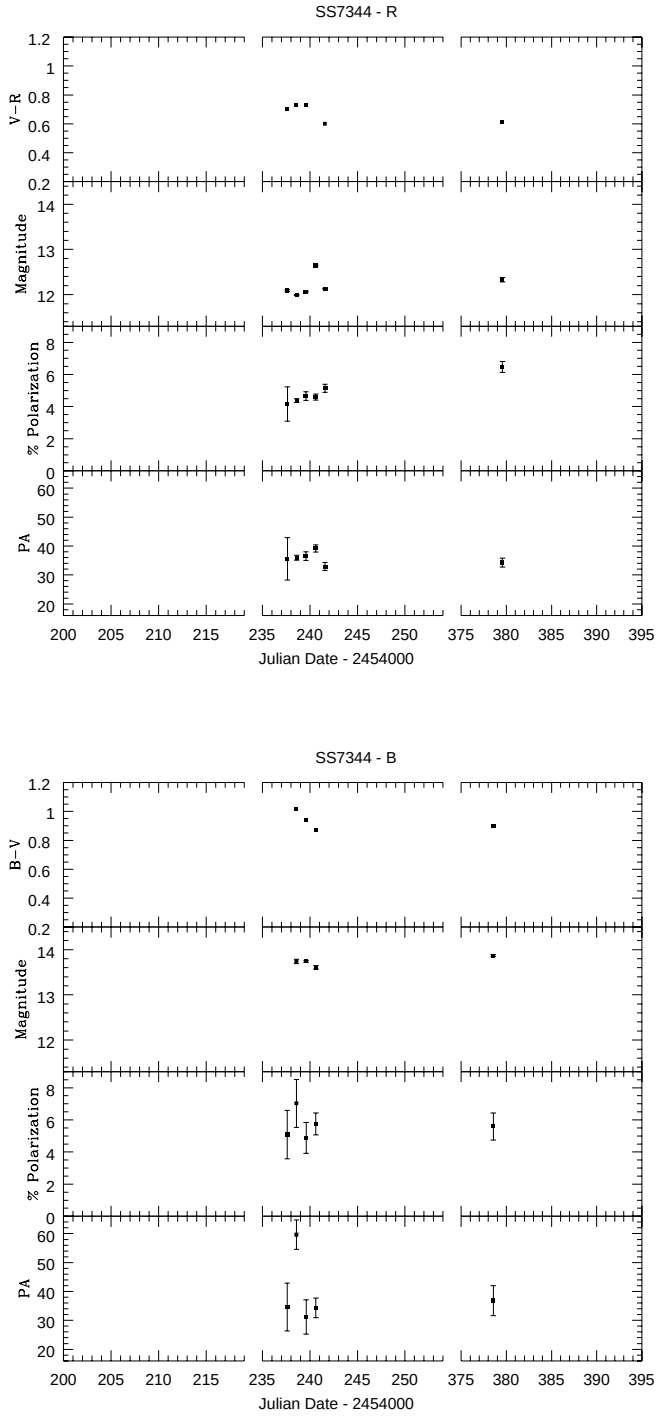

Figure 5.16 Same as figure 5.15 except with the data from the R (top) and B (bottom) wavebands plotted separately for the nights in which multiple waveband observations exist.

second scenario, only a star seen virtually "edge-on" would be expected to demonstrate photometric and polarimetric variability.

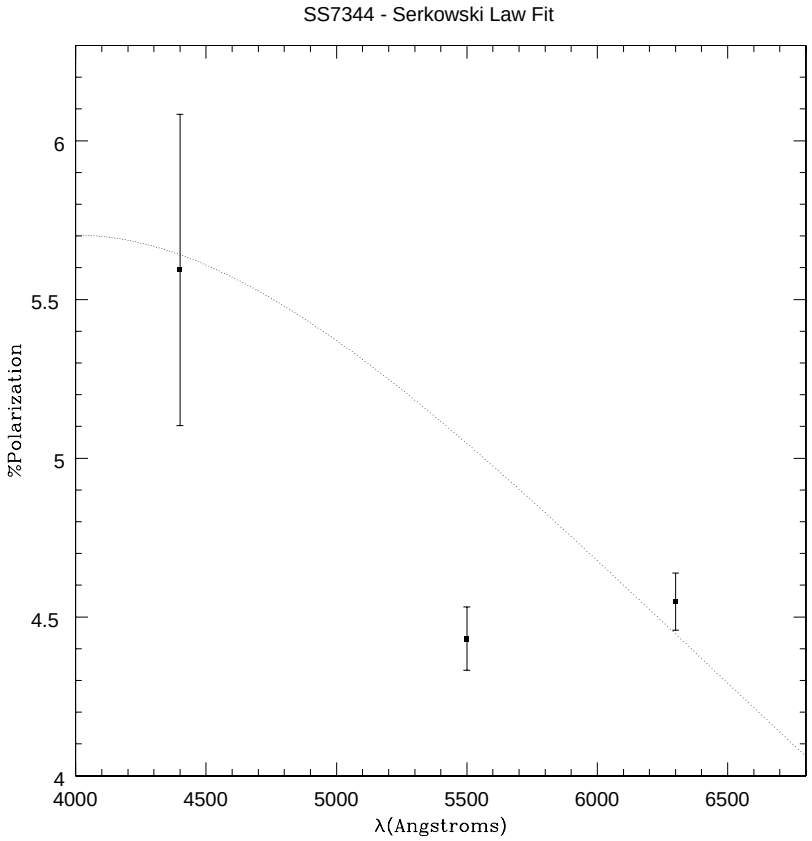

Figure 5.17 The polarization data of SS7344 as a function of wavelength. B, V, and R data points are shown. The dashed line indicates the Serkowski law. The fit to Serkowski's law is not good (the R^2 value is 0.86), indicating the presence of intrinsic polarization in this star.

5.6.4 Investigating the ISM of SS7344

The observation of Ray & Eisloeffel (1994) that there exist in the vicinity of SS7344 several HH outflows with a similar position angle led us to ask the question of whether the stars in the vicinity of SS7344 could be influenced in the same way by a large-scale magnetic field in the star-forming region. In order to answer that question, we

measured the polarization of several stars in the field of view of our SS7344 images, and compared the PA of their polarization vectors (which is presumably due to interstellar polarization), to the PA of SS7344's polarization vector, and to the PA of the HH outflow associated with the star. The results of this analysis are shown in figure 5.18.

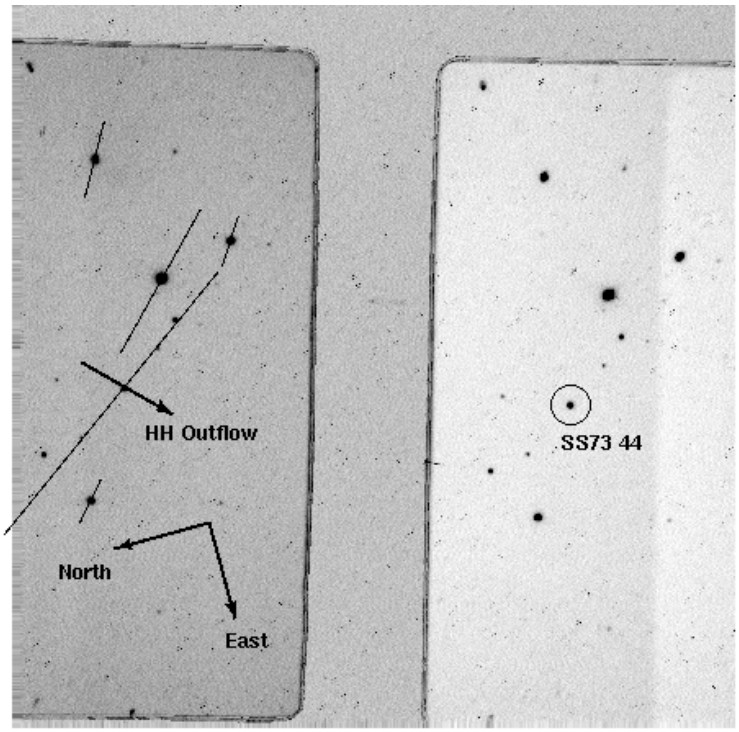

Figure 5.18 An analysis of the polarization values and position angles of stars in the region surrounding SS7344. The magnitude of the measured polarization is represented by the length of the line overlaying each star, while the PA of the polarization is represented by the orientation of the line. The polarization vector of SS7344 is roughly parallel to those of the surrounding stars, and roughly perpendicular to the observed HH outflow. This could be a result of a large-scale magnetic field influencing the orientation of disks in this star-forming region.

In order to draw definite conclusions about the presence of a magnetic field in the circinus cloud, the polarizations of more stars in the area would need to be measured. In particular, stars whose association with this star-forming region are certain would have to be observed to rule out the possibility of a component of polarization aris-

ing from outside of the cloud. However, the few measurements that we have made reveal the possibility of interesting magnetic structure in this region of the cloud. As shown in figure 5.18, the polarization vectors for all those stars measured are roughly (within 10°) parallel to each other, and these, in turn are roughly (again within 10°) perpendicular to the HH outflows observed by Ray & Eisloeffel (1994). While it is possible that this correlation is coincidental, it is also consistent with some theories of star formation that suggest that magnetic fields play an important role in the early evolution of stars (eg. Crutcher (1999)).

Chapter 6

Discussion

We have designed and built a low-cost imaging polarimeter using off-the-shelf components, and we have installed it permanently on one of the PROMPT telescopes at CTIO. We have then used the polarimeter to investigate the circumstellar environments of several HAEBE stars. In this section we will first discuss the results of the instrumentation project, followed by the results of the observing campaign.

6.1 The Polarimeter

The PROMPT polarimeter uses a Fresnel rhomb and wollaston prism to produce two side-by-side images of the two orthogonal polarization states. The wollaston prism has been placed within a re-imaging lens system to greatly reduce the effects of chromatic aberrations and focal plane curvature. A mask placed at the first image plane of the system constrains the area of the sky that is imaged onto the CCD and prevents excessive image overlap. The total cost of all the parts included in the polarimeter remained within our established budget.

The polarimeter images an area of 10' x 4'. This large image area makes the polarimeter ideal for follow-up observations on TOOs with large error circles. It also allows for the study of extended objects.

Mounted on a 16-inch (0.41-meter) Ritchy-Cretien OTA, the limiting V-magnitude of the polarimeter is 16.5 mag, and it can measure polarization levels down to 0.4%.

Typical error bars on polarization measurements are $\sim 0.2\%$ and $\sim 3°$, which match the errors associated with most other polarimeters in use today.

We have demonstrated the feasibility of constructing a low-cost polarimeter with off-the-shelf optics, and we have demonstrated that such an instrument can gather good-quality scientific data. Our experience with the PROMPT polarimeter has put us in a position to begin discussing whether we should invest the time to build a "mark 2" polarimeter that will improve upon the quality of the current instrument. The main argument in favor of building this "mark 2" instrument would be to re-design the optics so that the image overlap would be completely eliminated. The main argument against such an undertaking is the large investment of both money and time that would go into the improvement.

6.2 The UXor Effect

We have done an in-depth study of three HAEBE stars that were UXor candidates. All three stars exhibit some intrinsic polarization, but none of the three show the typical UXor behavior of increasing polarization and reddening with decreasing magnitude. We also have not observed a "blueing" effect at deep minima for any of the three stars. For all three stars, this study represents the most polarimetric data obtained to date, and for two of them (NX Pup and SS7344), this is the first instance of simultaneous polarimetry and photometry.

Although none of the stars should be classified as typical UXors, some of our observations do support the idea that dust obscuration events may be partially, if not totally, responsible for the observed changes in polarization. Both KK Oph and NX Pup show instances of increased polarization accompanied by a decrease in magnitude, although there are also times when the polarization increases without a corresponding decrease in magnitude. KK Oph also exhibits an increase in reddening with a decrease in magnitude, but we do not detect a "blueing" at deep minima. We note that we also did not detect the jump in position angle observed by Oudmaijer et al. (2001)

during which they observed both the faintest V-magnitude and the least polarization. As the polarization-producing mechanisms vary from star to star, we will discuss each of them individually.

6.2.1 KK Oph

KK Oph is the most well-studied star of our 3 chosen stars of interest, with extensive photometric data covering a 12-year period, as well as some limited prior polarimetric data.

We have observed KK Oph varying in both magnitude and polarization on a nightly basis, but our observations show no change in the position angle over a 6 month period. This indicates that the geometry of the region producing the polarization remains unchanged. We also detect no periodicity in the fluctuations of either the magnitude or the polarization of this star.

We have observed KK Oph in a state where it is at the extreme faint and red edge of the color-magnitude diagram. While we have observed a trend of increased reddening with decreased magnitude, we have not seen the "blueing" turnaround that has been reported for this star. However, we note that the EXPORT data shows KK Oph in a very blue state, with an increased polarization ($\sim 6.5\%$ compared to our observed values of $\sim 2 - 4.5\%$) but a similar position angle (Oudmaijer et al. 2001). At no time did we detect the 20° change in position angle observed by Oudmaijer et al. (2001).

A disk inclination angle of 70° has been derived by Leinert et al. (2004) for KK Oph, based on fitting VLTI mid-IR data to the models of Dullemond et al. (2001). Such an inclination is consistent with our observations - we see evidence of dust obscuration that is most easily explained by the presence of a highly inclined disk. The nearly nightly changes in both polarization and magnitude of this star imply a turbulence in the geometry of the dust, either in the form of a turbulent inner rim, or as a dusty outflow component.

Our observations of the star becoming very faint and very red without also becom-

ing more polarized are best explained by the "self-shadowed" disk models, in which the disk is not illuminated at all times by stellar light due to the presence of a puffed-up inner rim (Dullemond et al. 2003). Instances of increased polarization and blueing compared to the redder, less polarized states are not accompanied by a further decrease in magnitude, possibly because while the direct stellar light continues to be blocked by the rim, turbulence in the rest of the disk's rim allows for a partial illumination of the disk at these times. If this is the correct interpretation of our observations, then a dusty outflow component is not needed to explain the behavior of this star.

6.2.2 NX Pup

NX Pup is a star for which a multitude of photometric data exists (from LTVP, Manfroid et al. (1991)) but prior to this study, nearly no polarimetric data. In addition to the photometric monitoring, a combination of speckle masking and adaptive optics imaging of NX Pup have revealed it to have a close binary companion (separation 126 mas = 60 AU) (Schoeller et al. 1996). Despite the results of these two studies, the nature of NX Pup remains very much a mystery.

The imaging of NX Pup's companion was carried out under the assumption that the binary system was at an inclination of 0°, however Schoeller et al. (1996) show that comparison of the imaging results from 1993, 1995, and 1996 do no display any evidence for orbital motion. This result suggests either that the inclination $\neq 0°$, that the eccentricity > 0, or that the distance to NX Pup is considerably larger than 450 pc. The question of which condition has been assumed in error is still open. The color-magnitude diagram of NX Puseparatep is also puzzling. The CMD has an envelope parallel to the redding vector, so that color-magnitude variations along this line can be explained by circumstellar extinction. However, in the regions not along this line NX Pup seems to show no preferred towards any color as a function of brightness (Bibo & The 1991).

Like KK Oph, NX Pup is a highly variable star, varying in both polarization and in magnitude on a nightly basis. However, unlike KK Oph, the position angle of

the polarization of NX Pup also varies on a nightly basis. This is an indication of a changing geometry in the polarization-producing region, perhaps in association with two components of polarization, each with its own PA.

Our observations of NX Pup show a general trend of increased polarization with a decrease in magnitude. However, a look at the short-scale fluctuations reveals a more complicated picture. During the March observations (JD 170-185), the % polarization stays relatively constant while the PA and magnitude vary in an uncorrelated way. During the April observations (JD 200-220) the magnitude and PA seem to be correlated while the % polarization is anti-correlated with them both. Finally, in the May observations (JD 236-246) the magnitude again seems to correlate with the PA in all 3 wavebands, but the polarization is sometimes correlated and sometimes anti-correlated to their fluctuations.

The best explanation for our observations is that NX Pup is a system dominated by more than one source of polarization. Our observations indicate that it is not likely that the inclination of the system is at 0°, since there is evidence of a variable obcuration mechanism, and even dusty halo outflows tend to concentrate closer to the plane of the disk. The observation that the position angle fluctuates between the PA of the binary separation and the PA of the interstellar medium is also interesting. It is likely that the secondary star plays several roles in the polarization mechanism, by influencing the shape of the cicumstellar disk of the primary, and possibly by illuminating that disk even when the primary is partially obscured.

6.2.3 SS7344

SS73 44 is the least well-studied star in our sample. Based on the limited information that existed prior to this study, it would be reasonable to expect this star to be orbited by a circumstellar disk: not only are disks common to young stellar objects found in star-forming regions, but also the presence of Herbig-Haro objects associated with the star indicate the presence of an accretion disk and polar jet outflow. The luminosity of SS73 44 places it in the group of high-L HAEBE objects, and the

observation of P-Cygni profiles confirms that this star is subject to stellar winds.

SS7344 is a star that has intrinsic polarization, yet that polarization varies only slowly in B, V and R, aside from a single observation of an increased polarization with an accompanied change in position angle in the B waveband. The change in position angle during this observation implies that the polarization was produced in a different region than that observed throughout the remainder of the observations, and it could have been the result of turbulence or shocking in the polar jet or in the stellar wind.

The presence of Herbig-Haro objects in the vicinity of this star (Ray & Eisloeffel 1994) implies the presence of a disk, yet we see no polarization signature that indicates that the disk is at high inclination. However, the distribution of the HH objects argues against a disk seen at 0° inclination. Our data suggests that SS73 44 has a disk oriented at a low inclination, with little dust in the immediate circumstellar region. The possibility that the orientation of the disk has been influenced by the magnetic field of the star-forming region deserves further measurements.

6.3 Future Work

We have demonstrated the feasibility of studying HAEBE stars with the PROMPT polarimeter. Due to its robotic nature, the polarimeter is ideal for long-term studies - once its software is fully completed it can be programmed to collect nightly data and then carry out its observations without any other human interaction. Long-term simultaneous polarimetry and photometry of these very interesting stars would be extremely desirable to constrain the true nature of their circumstellar environments. If combined with NIR observations, this type of data would be very valuable for probing the circumstellar environments of young stars (as in Eiroa et al. (2002) and references therein).

Appendix A

Polarimetry Analysis: Determining %P and θ

This section is a step-by-step guide to determining the percent polarization and polarization angle, once the flux values of the source being analyzed are known in all acquired images. In practise, these calculations will most likely be done by a spreadsheet program or with the aid of some simple code.

A.1 Data

After reduction, the polarimetry data will consist of 4 images representing the 4 positions of the polarimeter at the time of image acquisition (0°, 45°, 22.5° and 67.5°). Each of these images has a left and a right side, so there are a total of 8 different flux values of the source being analyzed (0°L, 0°R, 45°L, 45°R, ...). The flux value is the value returned by IRAF as "flux" in the aperture photometry program apphot, and is calculated as:

$$\text{Flux} = \text{sum} - \text{area} * \text{msky} \tag{A.1}$$

where sum is the total number of counts in the aperture including sky, area is the area of the aperture in square pixels, and msky is the best estimate of the sky value

per pixel.

A.2 The Balance factor

The balance factor, ω, is defined as:

$$\omega \equiv \frac{I_A}{I_B} \tag{A.2}$$

which is the intensity ratio of the two retarder states used to determine a given Stokes' parameter. For Q, $A = 0°$ and $B = 45°$ and for U, $A = 22.5°$ and $B = 67.5°$. In theory, these two intensities should be equal, but in practice $I_A \neq I_B$ due to guiding errors and transparency changes. In terms of the measured flux values, ω is calculated as:

$$\omega_q \equiv \frac{I_{0°}}{I_{45°}} = \sqrt{\frac{(\text{Flux})_{0°R} \cdot (\text{Flux})_{0°L}}{(\text{Flux})_{45°R} \cdot (\text{Flux})_{45°L}}} \tag{A.3}$$

$$\omega_u \equiv \frac{I_{22.5°}}{I_{67.5°}} = \sqrt{\frac{(\text{Flux})_{22.5°R} \cdot (\text{Flux})_{22.5°L}}{(\text{Flux})_{67.5°R} \cdot (\text{Flux})_{67.5°L}}} \tag{A.4}$$

A.3 Calculating the Stokes' Parameters

Here we assume that the light entering the retarder may be represented by a total intensity, I, and two fractions p_0 and p_{90} representing the fraction of light with a polarization state at 0° and at 90° respectively ($p_0 + p_{90} = 1$). Then values of the normalized Stokes parameters q and u may be calculated for each of the right- and left-hand sides as follows.

$$q_L = \frac{I_{0°}p_0 - I_{45°}p_{90}}{I_{0°}p_0 + I_{45°}p_{90}} = \frac{(\text{Flux})_{0°L} - \omega_q(\text{Flux})_{45°L}}{(\text{Flux})_{0°L} + \omega_q(\text{Flux})_{45°L}} \tag{A.5}$$

$$q_R = \frac{I_{45°}p_0 - I_{0°}p_{90}}{I_{45°}p_0 + I_{0°}p_{90}} = \frac{\omega_q(\text{Flux})_{45°R} - (\text{Flux})_{0°R}}{\omega_q(\text{Flux})_{45°R} + (\text{Flux})_{0°°R}} \tag{A.6}$$

$$u_L = \frac{I_{22.5^\circ} p_0 - I_{67.5^\circ} p_{90}}{I_{22.5^\circ} p_0 + I_{67.5^\circ} p_{90}} = \frac{(\text{Flux})_{22.5^\circ L} - \omega_u (\text{Flux})_{67.5^\circ L}}{(\text{Flux})_{22.5^\circ L} + \omega_u (\text{Flux})_{67.5^\circ L}} \tag{A.7}$$

$$u_R = \frac{I_{67.5^\circ} p_0 - I_{22.5^\circ} p_{90}}{I_{67.5^\circ} p_0 + I_{22.5^\circ} p_{90}} = \frac{\omega_u (\text{Flux})_{67.5^\circ R} - (\text{Flux})_{22.5^\circ R}}{\omega_u (\text{Flux})_{67.5^\circ R} + (\text{Flux})_{22.5^\circ R}} \tag{A.8}$$

Once these 4 values are calculated, the % polarization and polarization angle may be determined.

$$q = \frac{q_L + q_R}{2}, \qquad u = \frac{u_L + u_R}{2} \tag{A.9}$$

$$P = \sqrt{q^2 + u^2}, \qquad \theta = \frac{1}{2} \arctan \frac{u}{q} \tag{A.10}$$

Appendix B

Mechanical and Electrical Assembly

Mechanical Connections

Connected Components	Type of Connection
OTA - Filter Wheel	2", 24 TPI threaded mount
Filter Wheel - Goniometer & Rhomb	2, 1/4" adapter plates, 16 8-32 screws
Goniometer & Rhomb - Wollaston & Re-Imager	6 M5 screws
Wollaston & Re-Imager - Camera	7 M4 screws

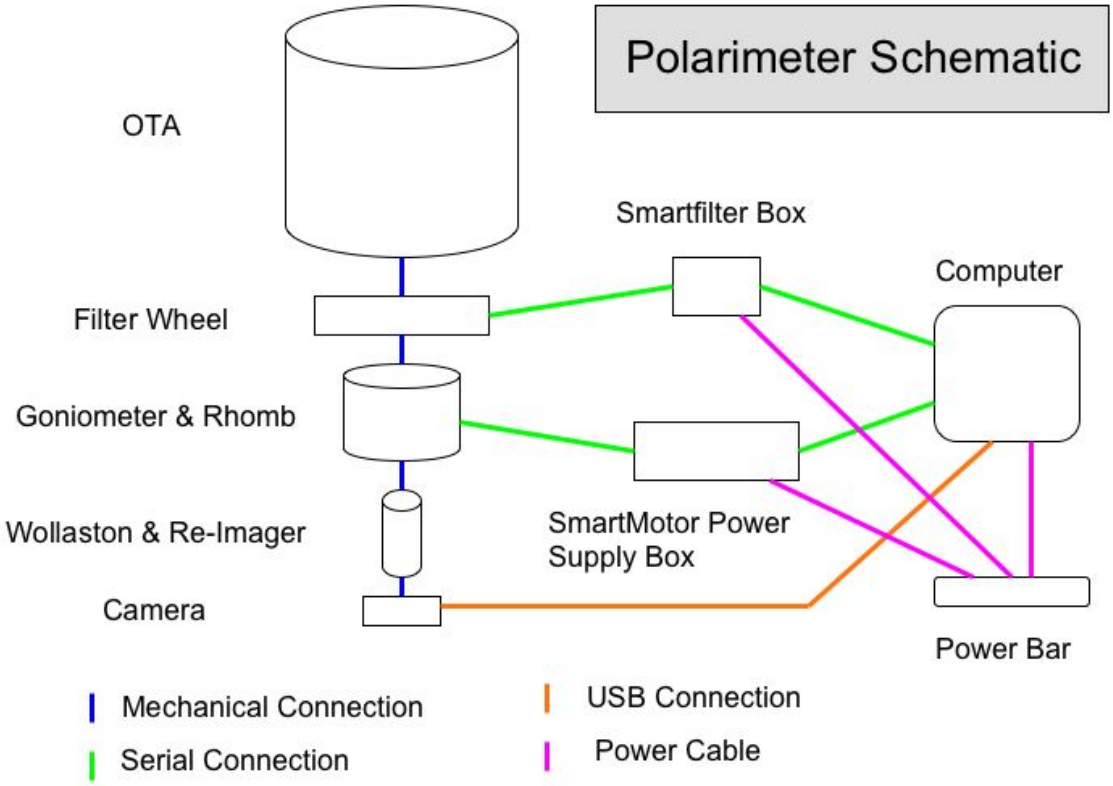

Figure B.1 A schematic diagram of the PROMPT polarimeter, showing the mechanical and electrical connections.

Serial Connections

Connected Components	Type of Connection
Filter Wheel - SmartFilter Box	Specialized 26 Pin cable, 140” long
Smartfilter Box - Computer	M/F DB9 cable, 10’ long
Goniometer - SmartMotor Power Box	Specialized DB9 cable, 208” long
Power Supply Box - Computer	M/F DB9 cable, 70” long

USB Connections

Connected Components	Type of Connection
Camera - Computer	USB Cable, 5m long (alta standard)

Power Cable Connections

Connected Components	Type of Connection
Smartfilter Box - Power Bar	120” Power cable
Power Supply Box - Power Bar	56” Power cable
Computer - Power Bar	70” + 72” cables with AC adapter

Appendix C

Filter Wheel and Goniometer Positioning

C.1 Filter Wheel Setup

Wheel 1 = Polarizing Filters

Wheel 2 = UBVRI Filters

Position	Wheel 1	Wheel 2
1	VIS-Polarizer	B
2	UV1-Polarizer	V
3	NIR2-Polarizer	R
4	E	E
5	E	E
6	E	E
7	E	E

Filter Wheel Commands (using hypertrm):

+	Full Status Command
UW	Using Wheel (1 UW or 2 UW)
MV	Move (0 MV, 1 MV, 2 MV, etc.)
CS	Check System (Rotates through all)
HM	Home (if wheel is out of position)
HELP	Help (lists commands)

C.2 Goniometer Positioning

The goniometer has a full range of 90°, but the fresnel rhomb only needs to rotate through a total of 67.5°. In order to keep the goniometer in the middle of its range (ie. as far from its limits as possible), we have adopted the positions shown in figure C.1 as standard.

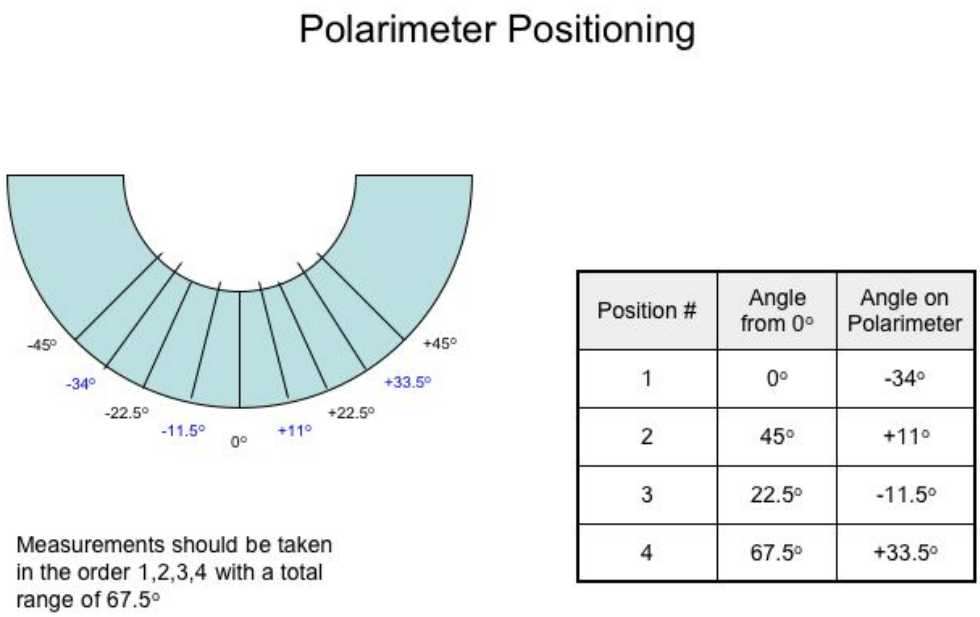

Figure C.1 The positioning adopted for the goniometer to keep the rotation as far from its limits as possible.

REFERENCES

Allen, D. A. 1978, MNRAS, 184, 601

Bally, J., Reipurth, B., Lada, C. J., & Billawala, Y. 1999, AJ, 117, 410

Bastien, P. 1981, A&A, 94, 294

—. 1987, ApJ, 317, 231

Bersier, D. et al. 2003, ApJ, 583, L63

Bertout, C. 2000, A&A, 363, 984

Bibo, E. A., & The, P. S. 1991, A&AS, 89, 319

Carmona, A., van den Ancker, M. E., & Henning, T. 2007, A&A, 464, 687

Chandrasekhar, S. 1960, Radiative transfer (New York: Dover, 1960)

Coburn, W., & Boggs, S. E. 2003, Nature, 423, 415

Covino, S. et al. 1999, A&A, 348, L1

Crutcher, R. M. 1999, ApJ, 520, 706

de Winter, D., van den Ancker, M. E., Maira, A., Thé, P. S., Djie, H. R. E. T. A., Redondo, I., Eiroa, C., & Molster, F. J. 2001, A&A, 380, 609

Dullemond, C. P., Dominik, C., & Natta, A. 2001, ApJ, 560, 957

Dullemond, C. P., van den Ancker, M. E., Acke, B., & van Boekel, R. 2003, ApJ, 594, L47

Eiroa, C. et al. 2002, A&A, 384, 1038

Eisner, J. A., Lane, B. F., Hillenbrand, L. A., Akeson, R. L., & Sargent, A. I. 2004, ApJ, 613, 1049

Gahm, G. F., & Malmort, A. M. 1980, A&A, 82, 295

Gledhill, T. M., Scarrott, S. M., & Wolstencroft, R. D. 1991, MNRAS, 252, 50P

Granot, J., & Königl, A. 2003, ApJ, 594, L83

Grinin, V. P. 2000, in Astronomical Society of the Pacific Conference Series, Vol. 219, Disks, Planetesimals, and Planets, ed. G. Garzón, C. Eiroa, D. de Winter, & T. J. Mahoney, 216–+

Grinin, V. P., Kiselev, N. N., Chernova, G. P., Minikulov, N. K., & Voshchinnikov, N. V. 1991, Ap&SS, 186, 283

Grinin, V. P., Kiselev, N. N., Minikulov, N. H., & Chernova, G. P. 1988, Pis ma Astronomicheskii Zhurnal, 14, 514

Grinin, V. P., & Kozlova, O. V. 2000, Astrophysics, 43, 239

Grinin, V. P., The, P. S., de Winter, D., Giampapa, M., Rostopchina, A. N., Tambovtseva, L. V., & van den Ancker, M. E. 1994, A&A, 292, 165

Hartmann, L., Kenyon, S. J., & Calvet, N. 1993, ApJ, 407, 219

Hecht, E. 1998, Optics (New York: Addison Wesley Longman, 1998, 3rd ed.)

Herbig, G. H. 1960, ApJS, 4, 337

—. 2005, AJ, 130, 815

Herbst, W., Herbst, D. K., Grossman, E. J., & Weinstein, D. 1994, AJ, 108, 1906

Herbst, W., & Shevchenko, V. S. 1999, AJ, 118, 1043

Hillenbrand, L. A., Strom, S. E., Vrba, F. J., & Keene, J. 1992, ApJ, 397, 613

Hsu, J.-C., & Breger, M. 1982, ApJ, 262, 732

Isella, A., & Natta, A. 2005, A&A, 438, 899

Isella, A., Testi, L., & Natta, A. 2006, A&A, 451, 951

Jackson, J. D. 1975, Classical electrodynamics (92/12/31, New York: Wiley, 1975, 2nd ed.)

Lazzati, D. et al. 2004, A&A, 422, 121

Leinert, C., Richichi, A., & Haas, M. 1997, A&A, 318, 472

Leinert, C. et al. 2004, A&A, 423, 537

Maheswar, G., Manoj, P., & Bhatt, H. C. 2002, A&A, 387, 1003

Manchado, A., Garcia-Lario, P., Sahu, K. C., & Pottasch, S. R. 1990, A&AS, 84, 517

Manfroid, J. et al. 1991, A&AS, 87, 481

—. 1995, A&AS, 109, 329

Monnier, J. D. et al. 2006, ApJ, 647, 444

Monnier, J. D., & Millan-Gabet, R. 2002, ApJ, 579, 694

Monnier, J. D. et al. 2005, ApJ, 624, 832

Mundell, C. G. et al. 2007, Science, 315, 1822

Natta, A., Grinin, V. P., Mannings, V., & Ungerechts, H. 1997, ApJ, 491, 885

Natta, A., & Whitney, B. A. 2000, A&A, 364, 633

Oliva, E. 1997, A&AS, 123, 589

Oudmaijer, R. D. et al. 2001, A&A, 379, 564

Pereira, C. B., Franco, C. S., & de Araújo, F. X. 2003, A&A, 397, 927

Piirola, V. 1975, Ann. Acad. Sci. Fennicae, Ser. A, VI. Phys., No. 418, 61 p., 418, 1

Pirzkal, N., Spillar, E. J., & Dyck, H. M. 1997, ApJ, 481, 392

Ramaprakash, A. N., Gupta, R., Sen, A. K., & Tandon, S. N. 1998, A&AS, 128, 369

Rautela, B. S., Joshi, G. C., & Pandey, J. C. 2004, Bulletin of the Astronomical Society of India, 32, 159

Ray, T. P., & Eisloeffel, J. 1994, A&A, 290, 605

Reichart, D. et al. 2005, Nuovo Cimento C Geophysics Space Physics C, 28, 767

Rol, E. et al. 2000, ApJ, 544, 707

Rossi, E. M., Lazzati, D., Salmonson, J. D., & Ghisellini, G. 2004, MNRAS, 354, 86

Rutledge, R. E., & Fox, D. B. 2004, MNRAS, 350, 1288

Sandqvist, A. 1977, A&A, 57, 467

Sanduleak, N., & Stephenson, C. B. 1973, ApJ, 185, 899

Scalise, Jr., E., Gahm, G. F., & Sandell, G. 1981, A&A, 104, 166

Scarrott, S. M., Warren-Smith, R. F., Pallister, W. S., Axon, D. J., & Bingham, R. G. 1983, MNRAS, 204, 1163

Schoeller, M., Brandner, W., Lehmann, T., Weigelt, G., & Zinnecker, H. 1996, A&A, 315, 445

Serkowski, K. 1973, in IAU Symposium, Vol. 52, Interstellar Dust and Related Topics, ed. J. M. Greenberg & H. C. van de Hulst, 145–+

Serkowski, K., Mathewson, D. S., & Ford, V. L. 1975, ApJ, 196, 261

Shakhovskoj, D. et al. 2006, A&A, 448, 1075

Shakhovskoj, D. N., Grinin, V. P., & Rostopchina, A. N. 2005, Astrophysics, 48, 135

Shevchenko, V. S., Grankin, K. N., Ibragimov, M. A., Melnikov, S. Y. U., & Yakubov, S. D. 1994, in Astronomical Society of the Pacific Conference Series, Vol. 62, The Nature and Evolutionary Status of Herbig Ae/Be Stars, ed. P. S. The, M. R. Perez, & E. P. J. van den Heuvel, 47–+

Sterken, C. et al. 1993, A&AS, 102, 79

—. 1995, A&AS, 113, 31

The, P. S., de Winter, D., & Perez, M. R. 1994, A&AS, 104, 315

Trammell, S. R. 1994, PhD thesis, AA(THE UNIVERSITY OF TEXAS AT AUSTIN.)

Tuthill, P. G., Monnier, J. D., & Danchi, W. C. 2001, Nature, 409, 1012

Vinković, D., Ivezić, Ž., Jurkić, T., & Elitzur, M. 2006, ApJ, 636, 348

Vinković, D., & Jurkić, T. 2007, ApJ, 658, 462

Whitney, B. A., & Hartmann, L. 1992, ApJ, 395, 529

Wijers, R. A. M. J. et al. 1999, ApJ, 523, L33

Yudin, R. V. 2000, A&AS, 144, 285

Yudin, R. V., & Evans, A. 1998, A&AS, 131, 401